Author Manuscript

Author Manuscript

Author Manuscript

Author Manuscript

HHS Public Access

Author manuscript

Cell Rep. Author manuscript; available in PMC 2024 July 11.

Published in final edited form as:

Cell Rep. 2024 May 28; 43(5): 114176. doi:10.1016/j.celrep.2024.114176.

PRMT1 promotes epigenetic reprogramming associated with acquired chemoresistance in pancreatic cancer

Chan D.K. Nguyen[1], **Benjamín A. Colón-Emeric**[1], **Shigekazu Murakami**[1], **Mia N.Y. Shujath**[1], **Chunling Yi**[1,2,*]

[1]Lombardi Comprehensive Cancer Center, Georgetown University Medical Center, Washington, DC, USA

[2]Lead contact

SUMMARY

Pancreatic ductal adenocarcinoma (PDAC) carries a dismal prognosis due to therapeutic resistance. We show that PDAC cells undergo global epigenetic reprogramming to acquire chemoresistance, a process that is driven at least in part by protein arginine methyltransferase 1 (PRMT1). Genetic or pharmacological PRMT1 inhibition impairs adaptive epigenetic reprogramming and delays acquired resistance to gemcitabine and other common chemo drugs. Mechanistically, gemcitabine treatment induces translocation of PRMT1 into the nucleus, where its enzymatic activity limits the assembly of chromatin-bound MAFF/BACH1 transcriptional complexes. Cut&Tag chromatin profiling of H3K27Ac, MAFF, and BACH1 suggests a pivotal role for MAFF/BACH1 in global epigenetic response to gemcitabine, which is confirmed by genetically silencing MAFF. PRMT1 and MAFF/BACH1 signature genes identified by Cut&Tag analysis distinguish gemcitabine-resistant from gemcitabine-sensitive patient-derived xenografts of PDAC, supporting the PRMT1-MAFF/BACH1 epigenetic regulatory axis as a potential therapeutic avenue for improving the efficacy and durability of chemotherapies in patients of PDAC.

In brief

Nguyen et al. investigate mechanisms of acquired chemotherapy resistance in pancreatic ductal adenocarcinoma (PDAC). By identifying the PRMT1-MAFF/BACH1 axis as a key mechanism of response to chemotherapy, Nguyen et al. demonstrate a promising pathway for improving the efficacy of chemotherapy treatments in PDAC.

This is an open access article under the CC BY-NC-ND license (https://creativecommons.org/licenses/by-nc-nd/4.0/).

*Correspondence: cy232@georgetown.edu.

AUTHOR CONTRIBUTIONS

C.Y. conceived and supervised the project. C.D.K.N. and C.Y. designed the experiments, conducted the analysis, and wrote the manuscript. C.D.K.N., B.A.C.-E., S.M., and M.N.Y.S. conducted a subset of the experiments and analysis presented. All authors reviewed and approved the final manuscript.

DECLARATION OF INTERESTS

The authors declare no competing interests.

SUPPLEMENTAL INFORMATION

Supplemental information can be found online at https://doi.org/10.1016/j.celrep.2024.114176.

Author Manuscript Author Manuscript Author Manuscript Author Manuscript

Graphical abstract

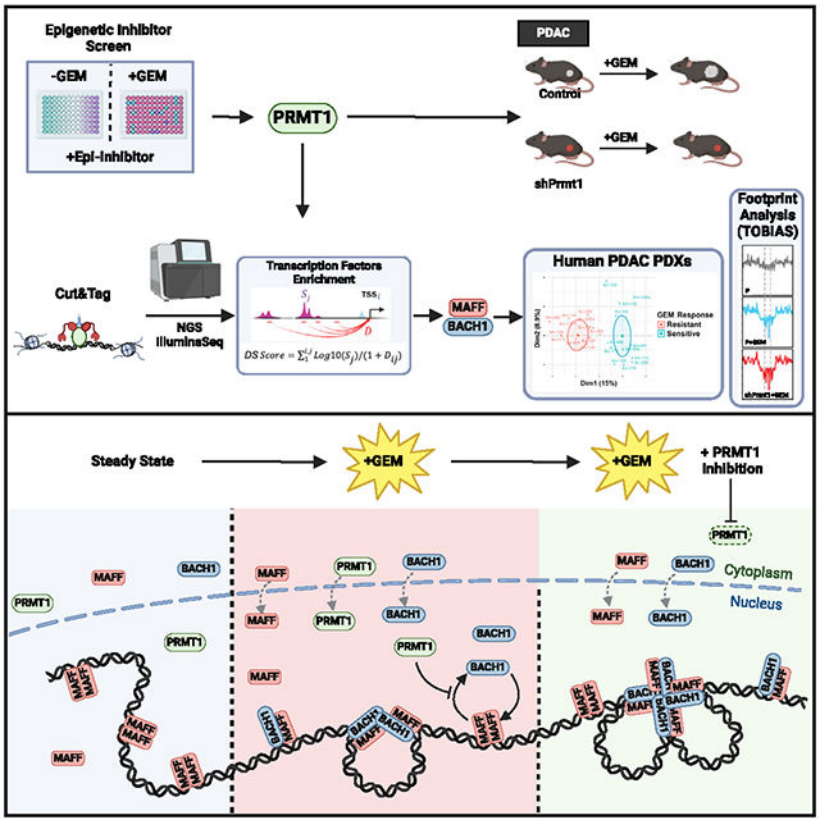

INTRODUCTION

Pancreatic ductal adenocarcinoma (PDAC) represents a major threat to public health, responsible for >48,000 deaths every year in the US alone.[1] Despite incremental improvement in overall outcomes, average 5-year survival rate remains around 10% with a median survival of 6 months.[1] While other aggressive cancers have benefited from breakthroughs in targeted and immune therapies, PDAC treatment remains dependent on chemotherapy such as combinations of gemcitabine (GEM), albumin-bound paclitaxel (ab-PAC) or FOLFIRINOX (composed of folinic acid, 5-fluorouracil [5-FU], irinotecan, and oxaliplatin) as standard first-line treatments for locally advanced and metastatic PDAC.[2,3] Approximately 77% of patients with PDAC present with upfront (intrinsic) resistance to FOLFIRINOX or the GEM/ab-PAC combination, while 23% develop acquired resistance following partial response.[2]

Epigenetic reprogramming is a fundamental process imparting non-genetic information across generations of cells through DNA methylation and post-translational modifications (PTMs) of histones, and it is choreographed by a large number of epigenetic regulators including “readers,” “writers,” and “erasers.”[4,5] Emerging evidence suggests that, during the process of acquiring resistance, cancer cells undergo epigenetic changes, adopting a more plastic and indolent phenotype similar to stem cells, known as drug-tolerant persisters

Author Manuscript Author Manuscript Author Manuscript Author Manuscript

(DTPs), which survive and eventually re-enter the cell cycle in the presence of drugs.[6,7] In the clinic, patients who developed acquired resistance to the GEM/ab-PAC combination experienced a rechallenge response following drug holidays, suggesting that acquired chemoresistance is a reversible process potentiated by epigenetic mechanisms.[8]

Here, we utilized cleavage under targets and tagmentation (Cut&Tag) followed by next-generation sequencing (NGS) to establish the progressive changes in epigenetic landscape during the process of acquiring GEM resistance in PDAC cells. Through a focused inhibitor screen targeting all major classes of epigenetic regulators, we identified protein arginine methyltransferase 1 (PRMT1) as a central driver of acquired GEM resistance in PDAC cells, and further showed that PRMT1 promotes adaptive epigenetic reprogramming to chemotherapy by regulating the chromatin interaction kinetics of transcription factors.

RESULTS

Global epigenetic reprogramming is associated with acquisition of gemcitabine resistance in PDAC

To develop a model of acquired chemoresistance, we performed colony-formation assays on mT4[9] murine and MiaPaca2 human PDAC cells treated with various doses of GEM. As expected, higher concentrations of GEM significantly decreased the number of colonies formed, indicating selection of intrinsically resistant clones (Figure S1A). In contrast, lower doses of GEM slowed colony formation without significantly reducing colony numbers, implying gradual acquisition of GEM resistance of the overall cell population (Figure S1A). Further proliferation, cell cycle, and apoptosis assays confirmed that, in response to sub-lethal GEM, PDAC cells underwent acute S-phase arrest without significant cell death before resuming exponential growth despite continuous GEM treatment (Figures 1A, S1B, and S1C).

To determine whether acquired GEM resistance is accompanied by global epigenetic reprogramming, we conducted H3K27Ac Cut&Tag[10] and NGS analysis in mT4 PDAC cells treated with 15 nM GEM for 0, 2, 4, 6, 8, and 10 days, spanning the entire adaptation process of mT4 cells to GEM (Figure 1A). Multiple-dimension scaling (MDS)[11] of normalized H3K27Ac peak signals demonstrated that GEM treatment initially induced acute changes in global H3K27Ac signal profiles followed by gradual partial recovery and accumulation of novel changes over the 10-day period (Figure 1B). Among the 14,029 H3K27Ac peaks significantly upregulated or downregulated at any time point of GEM treatment relative to the untreated (D0) baseline ($|\text{fold change}| > 2$; adjusted $p < 0.05$), 41.6%, 35.4%, and 18.4% were located at intronic, intergenic, and promoter regions respectively (Figure 1C), similar to the overall genomic distribution of the total 21,911 detected H3K27Ac peaks (Figure S1D). Fuzzy C-means clustering[12] revealed three major change patterns among the differential H3K27Ac peaks: C1, acute increase followed by progressive decline; C2, gradual increase saturating between day 8 and day 10; and C3, early loss followed by partial or complete recovery by day 8 (Figure 1D). Using the Genomic Regions Enrichment of Annotations Tool (GREAT),[13] we performed Gene Ontology (GO) enrichment analysis of genes closest to enhancers and promoters belonging to each cluster. C1 was selectively enriched for genes involved in negative regulation of apoptosis; C2 was

Author Manuscript Author Manuscript Author Manuscript Author Manuscript

enriched for genes involved in transcription, negative regulators of biosynthesis, and stress response; while C3 was enriched for genes belonging to the intrinsic apoptotic signaling pathway (Table S1).

Because not all enhancers act on the closest genes and H3K27Ac signal at transcription start sites (TSSs) has been shown to correlate with transcription levels,[14] we also conducted gene set enrichment analysis (GSEA)[15,16] against differential H3K27Ac peaks located within 500 bp of known TSSs. Unsupervised clustering of pathways predicted by GSEA to be significantly up- or downregulated at any treatment time points relative to D0 indicated acute increases in genes involved in cell-cycle checkpoints (Cdc27, Ccne2, etc.) and DNA damage response (Md2m, Stag2, etc.) and corresponding decreases in processes/pathways required for cell proliferation (organelle biogenesis, protein transport, adipogenesis, MTORC signaling, and MYC target genes) upon exposure to GEM (Figure 1E; Table S2). In contrast, EMT-related genes (Fn1, Itga2, Itgb1, etc.) were enriched at both early and late stages of GEM response, while chromatin-modifying enzymes (Arid1b, Carm1, Kdm6a, etc.) and housekeeping genes (Hsp90ab1, Psmd7, etc.) were specifically associated with later reprogramming (Figure 1E; Table S2). Additionally, our analysis indicated that GEM treatment may cause early suppression of genes activated by UV or infrared (IR) radiation followed by a late increase of UV-downregulated genes (Figure 1E; Table S2). We confirmed GEM-induced change patterns in H3K27Ac signal at the TSSs of a subset of these genes in mT4 cells using H3K27Ac chromatin immunoprecipitation (ChIP) and showed via quantitative real-time qRT-PCR that transcription levels of these genes exhibited corresponding changes in MiaPaca2 following GEM treatment (Figure S1E).

Next, we compared the observed GEM-induced epigenetic changes with published pre- and post-treatment RNA sequencing (RNA-seq) data from 25 human PDAC patient-derived xenografts (PDXs) sensitive ($N = 12$) or resistant ($N = 13$) to GEM.[17] Unsupervised clustering of differentially expressed genes between GEM-sensitive and GEM-resistant PDXs following GEM treatment produced six major clusters: (A) selectively gained in the sensitive group, (B) commonly gained in both groups, (C) selectively gained in the resistant group, (D) selectively lost in the sensitive group, (E) commonly lost in both groups, and (F) selectively lost in the resistant group (Figure S1F). Strikingly, a large fraction of these GEM-induced differentially expressed genes in human PDXs, particularly those belonging to clusters A, C, D, and F, corresponded to genes whose TSS showed differential H3K27Ac signal following GEM treatment of mT4 cells as determined by Cut&Tag (Figure S1G).

An epigenetic inhibitor screen nominates PRMT1 as a potential driver of acquired gemcitabine resistance in PDAC

After establishing that epigenetic and transcriptional reprogramming are involved in acquiring GEM resistance, we performed a comprehensive epigenetic inhibitor (Epi) screen to identify epigenetic regulators key to this process (Figure 2A). To maximize detection of the combination effects, we titrated the concentration of each epigenetic inhibitor to a dose that caused more than 1 log2 fold decrease in viability as a single agent (Figure 2B). We considered a drug a hit only if there was (1) at least a 2-fold difference between Epi + GEM and DMSO + GEM, and (2) a statistically significant

Author Manuscript Author Manuscript Author Manuscript Author Manuscript

difference in Epi/DMSO log2 fold change (log2FC) between the +GEM and −GEM arms (Figures 2A and 2B; Table S3). Our primary screen in mT4 cells identified several classes of epigenetic inhibitors that significantly inhibited the development of GEM resistance, including class I histone deacetylase (HDAC) inhibitors (MI192, panobinostat, BRD4884, AR42), H3K9 methyltransferase inhibitors (UNC0638 and BIX01294), PRMT1 inhibitors (MS-023, furamidine, TC-E5003), and retinoic acid receptor (RAR) inhibitors (LE135, BMS493) (Figure 2B).

Selecting representative hits from the primary screen for validation in three commonly used human PDAC cell lines (AsPC1, Panc1, and MiaPaCa2), we titrated each epigenetic inhibitor, finding that only H3K27 methyltransferase inhibitor (DZNep) and type I PRMT inhibitor (MS023) dose-dependently reduced GEM resistance development in all three human PDAC lines, while type II PRMT inhibitor (SCG3027)[18] promoted the acquisition of GEM resistance in all three human PDAC lines (Figures 2C and 2D; Table S3). Because the primary target of DZNep, enhancer of zeste homolog 2 (EZH2), was previously linked to GEM resistance,[19] we focused our subsequent analysis on the PRMT protein family.

PRMTs, which use the cofactor S-adenosyl-L-methionine (SAM) as a methyl donor to modify arginine, can be divided into three subtypes based on their primary arginine methylation products (monomethylarginine [MMA], asymmetric dimethylarginine [ADMA], and symmetric dimethylarginine [SDMA]). Type I PRMTs (PRMT1–4, 6, and 8) catalyze both MMA and ADMA, type II PRMTs (PRMT5 and 9) catalyze both MMA and SDMA,[20–22] and type III PRMT (PRMT7) exclusively catalyzes MMA.[18] Similar to MS-023, a SAM uncompetitive type I PRMT inhibitor GSK3368715[23] with no demonstrable effect on type II and III PRMTs[24] also increased GEM sensitivity in human and murine PDAC cells (Figures S2A and S2B). Screening an additional panel of inhibitors that selectively target a subset of type I PRMTs[25–33] revealed that only inhibitors that block PRMT1 activities suppressed development of GEM resistance (Figure 2D; Table S3).

PRMT1 promotes acquired gemcitabine resistance through its enzymatic activity

We then engineered doxycycline (Dox)-inducible mT4 lines carrying two distinct Prmt1-targeting short hairpin RNAs (shRNAs) fused to red fluorescent protein (RFP). qRT-PCR and western blot (WB) analysis confirmed that both shRNAs induced robust Prmt1 knockdown (KD) accompanied by a decrease in global ADMA levels (Figures 3A, 3B, S2C, and S2D). We performed a competitive growth assay, mixing RFP− parental with RFP+ Prmt1-KD PDAC cells in a 1:1 ratio, culturing the cells to confluence in the presence or absence of GEM and measuring changes in the ratio of the two subpopulations via flow cytometry (FC) (Figure 3A). Prmt1-KD cells were depleted relative to parental cells in a dose-dependent manner following GEM treatment, recapitulating the effects of small-molecule PRMT1 inhibitors (Figures 3A, S2A, and S2B). Prmt1-KD mT4 cells also exhibited enhanced sensitivity to GEM compared to mT4 cells expressing a scramble control shRNA (shCtrl) (Figure 3B), ruling out viral infection as a possible cause of GEM sensitization.

To test whether the enzymatic activity of PRMT1 is necessary for promoting GEM resistance, we introduced a wild-type (WT) or an enzymatically dead mutant (E171Q)[34]

Author Manuscript Author Manuscript Author Manuscript Author Manuscript

human PRMT1 into Prmt1-KD mT4 cells. In WB and competitive cell growth assays, WT PRMT1 completely restored both global ADMA levels and the ability to acquire GEM resistance in PDAC cells (Figures 3C, 3D, and S2D). In contrast, enzymatically dead PRMT1 failed to rescue the global ADMA downregulation or GEM sensitization induced by Prmt1-KD (Figures 3C, 3D, and S2D), demonstrating that the arginine methyltransferase activity of Prmt1 is indispensable for promoting acquired GEM resistance. Interestingly, genetic or pharmacological inhibition of PRMT1 also inhibited the development of resistance to other chemo drugs commonly used to treat PDAC, including irinotecan, paclitaxel (Taxol), and 5-FU (Figures 3E, 3F, S2E, and S2F).

To test the effects of PRMT1 inhibition *in vivo*, we injected parental or Dox-inducible Prmt1-KD mT4 cells subcutaneously into syngeneic, immune-competent C57BL/6 mice. After tumors reached ~100 mm^3, continuous Dox-containing diet coupled with intraperitoneal (i.p.) injections with either GEM or saline control three times weekly were initiated. Recapitulating our *in vitro* observations, Prmt1 silencing alone had little effect on tumor growth, but, when combined with GEM, it significantly delayed tumor growth and increased overall survival compared to GEM single treatment (Figure 3G). Similarly, PRMT1 inhibitor GSK3368715 delayed development of GEM resistance in the human AsPC1 xenograft model (Figure S2G).

PRMT1 promotes acquired gemcitabine resistance through multiple mechanisms

Immunofluorescence (IF) analysis revealed significant increases in nuclear PRMT1 signal post GEM treatment across three murine and human PDAC lines (Figure S3A), suggesting that PRMT1 likely exerts its effects in promoting GEM resistance in the nucleus. Cell-cycle and apoptosis analysis on parental and Prmt1-KD mT4 cells, and on MiaPaca2 and AsPC1 cells treated with vehicle control or PRMT1 inhibitor GSK3368715, showed that Prmt1 inhibition did not increase apoptosis, instead prolonging the S-phase arrest induced by GEM (Figures S3B–S3D). Immunohistochemistry (IHC) analysis of mT4 tumors with cell-cycle marker CyclinD1 and apoptosis marker cleaved caspase 3 confirmed that Prmt1-KD prolonged GEM-induced cell-cycle arrest but did not affect apoptosis *in vivo* (Figure S3E). WB analysis against DNA damage response markers pH2AX and Rpa32 showed that both markers increased following 1 day of GEM treatment and returned to near-basal levels by day 5 in parental but not in Prmt1-KD mT4 cells (Figure S3F). Treatment of AsPC1 cells with GEM in the presence or absence of PRMT1 inhibitor GSK3368715 yielded similar results (Figure S3G). Interestingly, IHC analysis of control and Prmt1-KD mT4 tumors treated with saline or GEM showed that tumor fibrosis (as indicated by smooth muscle actin [SMA] staining) was unaffected by PRMT1 depletion, but T cell tumor infiltration was significantly increased (Figure S3E). Thus, augmenting DNA damage response, which may in turn enhance T cell recruitment, is potentially one of the roles PRMT1 plays in facilitating the development of acquired GEM resistance *in vivo*.

Based on our observations of dynamic changes in the chromatin landscape following GEM treatment (Figure 1) and previous studies linking PRMT1 to arginine methylation of histone and various transcription factors (TFs),[35,36] we hypothesized that PRMT1 may also modulate the process of adaptive epigenetic reprogramming in response to GEM

Author Manuscript Author Manuscript Author Manuscript Author Manuscript

treatment. To test this, we carried out H3K27Ac Cut&Tag on parental and Prmt1-KD cells before or after GEM treatment. First, we assessed the baseline effects of Prmt1 silencing by comparing H3K27Ac peak profiles between parental and the two independent Prmt1-KD lines without GEM treatment. From 1,315 differential H3K27Ac peaks induced by Prmt1-KD, we identified 253 genes whose TSSs exhibited significantly reduced H3K27Ac signal in response to Prmt1-KD and were among the top 50% variably expressed genes in The Cancer Genome Atlas (TCGA) Pancreatic Adenocarcinoma (PAAD) RNA-seq dataset (Figure S4A). Using this basal PRMT1 gene signature, we performed unsupervised clustering of the TCGA PAAD RNA-seq data, segregating the patients into four major clusters. One of the clusters expressed low levels of most basal PRMT1 signature genes (Low), while the other three exhibited high expression of a subset of PRMT1 signature genes (High-1, High-2, High-3) (Figure S4B). Remarkably, nine out the 10 patients with low overall PRMT1 signature survived past 5 years, compared to the 5%–25% 5-year average survival rates for the high expression groups (Figure S4B). Principal-component analysis (PCA) of the aforementioned RNA-seq data from 25 human PDAC PDXs[17] according to the pretreatment expression levels of our baseline PRMT1 signature genes largely separated the GEM-sensitive from GEM-resistant PDXs (Figure S4C), suggesting that basal PRMT1 activity could predict responses to GEM.

We then examined how silencing Prmt1 influences GEM-induced epigenetic reprogramming by comparing the normalized signals of all 8,054 differential H3K27Ac peaks across three conditions: untreated parental PDAC cells (P), parental PDAC cells treated with GEM (P + GEM), and Prmt1-KD PDAC cells treated with GEM (shP1 + GEM). We represented the directions and magnitudes in H3K27Ac changes from P to P + GEM to shP1 + GEM using a Hue-saturation-value (HSV) transformation plot, where each point corresponds to a specific genomic location. The color gradient and angle of each point from the top of the circle denote the direction of change at the genomic locus; the relative distance of the point from the center of the circle indicates the maximum absolute log2FC in H3K27Ac signals between any two of the three aforementioned conditions at the same site (Figure 4A). Representative change patterns corresponding to different angles are illustrated outside the HSV plot, and the bars show the frequency of genomic loci that follow a given pattern (Figure 4A). There were three major enriched patterns of GEM-induced signal changes: (1) a significant increase in Prmt1-KD but not in parental cells (~0°), (2) a moderate increase in parental cells and a significant increase in Prmt1-KD (~30°), and (3) an increase in parental but not in Prmt1-KD cells (90°–135°; Figure 4A). Notably, while differential H3K27Ac peaks not overlapping with known TSSs (hereafter referred as *cis*-regulatory elements [CREs], $N = 4,621$) were evenly distributed across all three change patterns, the majority of differential TSS peaks ($N = 3,433$) exhibited an increase in parental cells but not in Prmt1-KD cells after GEM treatment (Figure 4A).

To assess the clinical significance of these presumed PRMT1-regulated GEM response genes, we performed PCA analysis according to their expression fold changes following GEM treatment in above-described human PDAC PDXs 52. As expected, this set of genes completely segregated the GEM-sensitive from GEM-resistant PDXs (Figure 4B). Additionally, we observed strong concordance between selectively differentially expressed genes (DEGs) in the resistant PDXs post GEM treatment and differential TSS peaks unique

Author Manuscript Author Manuscript Author Manuscript Author Manuscript

to GEM-treated parental but not Prmt1-KD cells (clusters A and C, Figures S4D and S4E). Similarly, DEGs detected specifically in sensitive PDXs post GEM treatment were strongly enriched with TSS peaks differentially regulated in GEM-treated Prmt1-KD but not parental cells (Clusters B and D, Figure S4D). These results suggest a prominent role for PRMT1-mediated epigenetic and transcriptional reprogramming in driving acquired GEM resistance in patients.

PRMT1 controls the dynamic recruitment of TFs to chromatin in response to gemcitabine

To identify TFs that may mediate PRMT1-dependent epigenetic and transcriptional responses to GEM, we calculated a distance-signal (DS) score[37] for every TF motif corresponding to at least one expressed TF by summing the values of the log10-transformed H3K27Ac signal of each CRE peak containing that TF motif, divided by the distance from the center of the CRE peak to each of the differential TSSs located on the same chromosome in parental, parental + GEM or shPrmt1 + GEM samples (Figure 4C). Differential enrichment of the DS scores across the three samples identified a number of TF motifs enriched in GEM-treated parental but not Prmt1-KD cells (Figure 4D), suggesting that these TFs may contribute to acquired GEM resistance in a PRMT1-dependent manner.

To follow up, we filtered the TFs to select those that had both existing literatures connecting them to PDAC[38–47] and available, validated commercial antibodies. We extracted the chromatin-enriched fractions from parental or Prmt1-KD mT4 cells treated with GEM from 0 to 14 days and performed WB analysis against representative members of these selected TF families, including SMAD, MAF, TEAD, SREBP, HIF, and GLI. While HIF1/2a and GLI1/3 were minimally detected in the chromatin fraction (not shown), all remaining TFs analyzed, including Smad2/3, MafF/G, pan-Tead, and Srebp2, displayed dynamic changes in chromatin binding during GEM treatment. On one hand, pan-Tead and Srebp2 displayed progressive increase in chromatin binding in parental cells but largely remained at basal levels in Prmt1-KD cells (Figure 4E), implying that Prmt1 is necessary for their chromatin recruitment in response to GEM. By contrast, Smad2/3 and MafF/G exhibited dramatic early increases in chromatin binding after 2 or 4 days of GEM treatment in parental cells, followed by gradual return to pre-treatment level starting from day 8 (Figure 4E). While Prmt1-KD had little effect on the initial chromatin recruitment of Smad2/3 and MafF/G after exposure to GEM, it prolonged chromatin retention of these TFs past 12 days of GEM treatment (Figure 4E). These results suggest that Prmt1 promotes the dissociation of Smad2/3 and MafF/G from the chromatin after extended GEM exposure.

PRMT1 drives acquired gemcitabine resistance in part by suppressing the nuclear accumulation of small MAF proteins and their hetero-oligomerization with BACH1

Given the prior literature implicating TEAD, SREBP, and SMAD in GEM resistance,[48–50] we focused our subsequent analysis on the small MAF (sMAF) subfamily of basic leucine zipper (bZIP) TFs, which, to our knowledge, have not been linked to GEM resistance. Through their bZIP domains, sMafs (MafF, MafG, and MafK) form either homodimers[51] or heterodimers with other bZIP subfamilies of TFs, particularly the “cap ‘n’ collar” (CNC) and the BTB and CNC homology (BACH) subgroups.[52–55] sMafs do not possess transactivation domains; they function exclusively as repressors when homodimerized but

Author Manuscript Author Manuscript Author Manuscript Author Manuscript

can either activate or repress transcription when hetero-dimerized/oligomerized with CNC (Nrf1, Nrf2, Nrf3) and BACH (Bach1 and Bach2) proteins (which cannot bind to DNA by themselves[52–54,56]). Among the CNC/BTB proteins, Bach1 alone exhibited detectable chromatin binding by WB in mT4 cells (Figures 4E and S5A). Upon exposure of parental or shCtrl mT4 cells to GEM, Bach1 was recruited to the chromatin in two waves: (1) an early peak between days 2 and 4 matching MafF and MafG peaks, and (2) a late recruitment after total levels of chromatin-bound MafF/G returned to near baseline (Figures 4E and S5A). Intriguingly, Prmt1-KD significantly increased levels of chromatin-bound Bach1 at all time points (including baseline) compared to parental or shCtrl controls, suggesting that Prmt1 inhibits Bach1 chromatin binding independent of GEM (Figures 4E and S5A). Prmt1-KD also enhanced chromatin recruitment of Bach1 in response to 5FU or paclitaxel, although its effects on Maff are less pronounced compared to GEM treatment (Figures S5B and S5C).

To determine whether chemo-induced dynamic chromatin recruitment of sMAFs and Bach1 resulted from increased protein buildup in the nucleus, we assessed the distributions of PRMT1, MAFF, and BACH1 within the cytoplasmic, total nuclear, and soluble and insoluble nuclear (chromatin) fractions of mT4 and AsPC1 cells during the course of GEM treatment by WB. Matching the IF results (Figure S3A), GEM gradually elevated soluble and insoluble nuclear PRMT1 levels (Figures 5A, S5D, and S5E). Similarly, GEM treatment also induced chromatin-bound MAFF and BACH1 in both cell lines (Figures 5A, S5D, and S5E). qRT-PCR and WB analysis in parental and Prmt1-KD mT4 cells in the presence or absence of GEM showed that Prmt1-KD did not consistently alter mRNA or total protein levels of either MafF or Bach1, but it markedly enhanced nuclear accumulation of MafF (Figures 5B and 5C). This effect was recapitulated by GSK3368715 treatment in MiaPaca2 and AsPC1 cells (Figure S5F). Since Bach1 requires sMaf to bind to DNA, we tested whether Prmt1 modulates Bach1 chromatin recruitment by regulating its interaction with sMaf. Co-immunoprecipitation (coIP) assay with MafF antibody in parental, shCtrl, or shPrmt1 mT4 cells with or without GEM treatment revealed that, while Prmt1-KD significantly increased levels of MafF-bound Bach1, this effect was independent of GEM treatment (Figures 5D and S5G). Once again, GSK3368715 recapitulated the effect of Prmt1-KD by increasing BACH1-MAFF association in MiaPaca2 cells (Figure S5H). These results indicate that Prmt1 counters GEM-induced chromatin buildup of MafF and Bach1 by inhibiting their Bach1/MafF hetero-oligomerization in the nucleus.

Genetic silencing of MAFF selectively desensitizes PDAC to gemcitabine regardless of PRMT1 inhibition

To test whether MafF is indeed a critical effector of Prmt1 in acquiring GEM resistance, we generated two independent MafF knockout (KO) mT4 lines (KO#1 and #2) and subjected them, along with parental control, to increasing concentrations of GEM in combination with a constant concentration of type I PRMT inhibitor GSK3368715 or vehicle control. MafF-KO mT4 cells became significantly more resistant to GEM in the presence or absence of GSK3368715 (Figures 5E, 5F, and S6A), confirming that Prmt1 promotes GEM resistance in large part by limiting MafF activity. We then investigated whether MafF also plays a general role in regulating chemoresistance. Unexpectedly, compared to parental cells, MafF-KO cells displayed enhanced sensitivities to paclitaxel, while maintaining similar responses

Author Manuscript Author Manuscript Author Manuscript Author Manuscript

to 5FU, irinotecan, and SN38 (active metabolite of irinotecan) (Figure 5F), effects that were recapitulated in MiaPaca2 cells (Figure S6B). These results indicate that, unlike Prmt1, MafF exerts divergent functions in response to different chemotherapeutic agents.

Gemcitabine treatment induces dynamic recruitment of MAFF and BACH1 to transcriptionally active and inactive genomic loci

To further explore the roles of MafF and its transcriptional partner Bach1 during GEM-induced epigenetic reprogramming, we performed MafF and Bach1 Cut&Tag using KO validated antibodies on mT4 cells collected at 2-day intervals following GEM treatment for up to 10 days (Figure S6A, S6C, and S6D) and compared their chromatin-binding dynamics to the corresponding H3K27Ac profiles. Consistent with the WB results above (Figure 4E), Cut&Tag analysis detected dynamic increases in the total numbers of MafF- and Bach1-binding sites at different time points during GEM treatment (Figure 6A). While most MafF peaks lacked Bach1 co-binding and were enriched at H3K27Ac− regions, Bach1 was almost exclusively recruited to pre-existing MafF sites at both H3K27Ac+ and H3K27Ac− loci (Figures 6A and S6E), an observation consistent with previous reports of MafF homodimers functioning exclusively as transcription repressors while the MafF/Bach1 hetero-oligomeric complex either activating or suppressing transcription.[52,54,57,58] Of the different sites bound by either MafF or MafF/Bach1, nearly 30% of MafF+Bach1+H3K27Ac+ sites were located at promoter-TSS regions, compared to 9% among MafF+Bach1−H3K27Ac− sites, 11% among MafF+Bach1+H3K27Ac− sites, and 22% among MafF+Bach1−H3K27Ac+ sites (Figure 6B). Furthermore, we observed high concordance in signal fluctuations across all GEM treatment time points between MafF, Bach1, and H3K27Ac at MafF+Bach1+H3K27Ac+ sites, particularly at promoter-TSS regions (Figures 6C and S6F), suggesting that the recruitment of Bach1 to MafF-bound active promoter-TSS regions potentially leads to increased transcription. We then extracted a list of genes whose promoter-TSS exhibited increased Bach1/MafF binding after prolonged GEM treatment and high Bach1-H3K27Ac and MafF-H3K27Ac signal concordance (Pearson correlation coefficiency >0.4 for both) (Figures S6F and S6G). Using the post-vs.-pre-treatment expression ratio of these genes, we re-performed PCA analysis of the human PDX mRNA sequencing data described above. Like PRMT1-regulated genes (Figure 4B), MafF/Bach1-associated genes were also able to separate GEM-resistant from GEM-sensitive PDXs (Figure S6H).

Chromatin-bound TFs protect their binding sites from Tn5 transposase cleavage, leaving so-called TF footprints (FPs) within the peaks detected by chromatin accessibility assays.[23] The depth of the FPs, defined as the corrected signal difference between the centers of the FPs and the immediate flanking regions, reflects the relative binding strength of the TF at the sites. sMafs bind to Maf recognition element (MARE) and closely related CNC/MAF response element (CsMRE) as homodimers or hetero-oligomeric complexes with CNC/BTB proteins.[53,55,57] To assess how GEM treatment affects the binding strengths of MafF and Bach1, we used TOBIAS[59] to perform Tn5-bias-corrected FP analysis of Bach1 and MafF Cut&Tag profiling data centered on the canonical MARE or CsMRE motifs at H3K27Ac+ or H3K27Ac− sites bound by either MafF alone or MafF/Bach1. Compared to Bach1/MafF co-bound sites, MARE or CsMRE motifs occupied by MafF alone exhibited shallow,

Author Manuscript Author Manuscript Author Manuscript Author Manuscript

largely unchanged FPs over the course of GEM treatment, regardless of H3K27Ac status (Figures 6D and S7A). At H3K27Ac− sites co-bound by MafF and Bach1, GEM treatment induced corresponding increases in the FP depths of both Bach1 and MafF (Figures 6D and S7A). In contrast, even though GEM treatment dramatically increased the overall signals of both Bach1 and MafF at H3K27Ac+ sites, it did not significantly alter their FP depths, implying little change in their binding affinities at these sites (Figures 6D and S7A). Finally, throughout GEM treatment, Bach1 left stronger FPs at H3K27Ac− sites relative to H3K27Ac+ sites, whereas MafF exhibited the opposite FP patterns (Figures 6D and S7A).

These data indicate that, at the basal state, MafF homodimers bind weakly to both H3K27Ac+ and H3K27Ac− sites in PDAC cells. GEM treatment promotes Bach1 recruitment to pre-existing MafF-bound sites, causing the switch from MafF-MafF to MafF-Bach1 heterodimers. MafF/Bach1 heterodimers exhibit stronger binding affinities at many H3K27Ac− sites due to increased anchoring by Bach1, presumably leading to further transcription suppression (Figure 6E). By contrast, the recruitment of Bach1 to the H3K27Ac+ sites pre-bound by MafF does not affect the binding strength of MafF to DNA; instead, it may induce the assembly of higher-order transcriptional complexes resulting in increased H3K27 acetylation and promoter/enhancer activities (Figure 6E).

PRMT1 acts as a brake to prevent overloading of the MAFF/BACH1 transcriptional complexes on chromatin in response to gemcitabine

Our WB analysis showed that Prmt1-KD increased chromatin-bound MafF and Bach1 in the presence of GEM (Figure 4E). To investigate whether this was caused by enhanced MafF/Bach1 binding affinities to existing sites or by their ectopic recruitment to noncanonical sites, we performed MafF and Bach1 Cut&Tag in parental mT4 cells treated with vehicle control and in GEM-treated parental and Prmt1-KD mT4 cells (P, P + GEM, shP1 + GEM). Of 8,862 Bach-bound sites detected in any of the three experimental conditions, 4,510 (51%) were found only in shPrmt1 + GEM, followed by 3,329 (38%) shared by P + GEM and shP1 + GEM (Figure S7). In contrast, the largest fraction of MafF peaks (16,966 out of 36,117, 47%) were detected in all three conditions (Figure S7B). Cut&Tag time course analysis indicated that GEM-induced Bach1 recruitment occurred primarily at MafF-bound genomic loci (Figure S6E). Seventy-four percent (2,453 out of 3,329) of Bach1 peaks commonly gained by GEM-treated parental and Prmt1-KD cells overlapped with MafF peaks detected across all three conditions (Figure S7B). By contrast, of 4,510 Bach1-binding sites unique to shP1 + GEM, 57% (2,568) were bound by MafF across all three conditions, 23.3% (890) were deprived of MafF in all of the conditions, 9.3% (419) concomitantly gained MafF binding in GEM-treated Prmt1-KD cells, and 6.9% (312) acquired MafF binding in GEM-treated parental and Prmt1-KD cells (Figure S7B). These results indicate that, while a majority of ectopic Bach1 chromatin binding induced by Prmt1-KD in combination with GEM occurred at sites pre-bound by MafF, there was also significant recruitment of Bach1 to genomic loci without prior MafF binding.

To test how Prmt1-KD affects Bach1 and MafF binding strength at each site, we performed HSV transformation of differential MafF (N = 20,017) and Bach1 (N = 6,332) peaks. Unlike H3K27Ac peaks, which were scattered around the HSV circle (Figure 4A), MafF peaks

Author Manuscript Author Manuscript Author Manuscript Author Manuscript

clustered mostly between 0° and 30°, indicating significant signal increase in shP1 + GEM compared to P and P + GEM (0°) or progressive signal increase across P, P + GEM, and shP1 + GEM (30°), while Bach1 peaks were highly concentrated around 30°, corresponding to progressive increase in Bach1 signals from P to P + GEM to shP1 + GEM (Figure 7A). Aggregating FP profiles of MafF and Bach1 at H3K27Ac− and H3K27Ac+ sites bound by either MafF alone or MafF/Bach1 across the three conditions showed that, without Bach1 co-binding, MafF exhibited shallow FPs minimally affected by GEM treatment or Prmt1-KD regardless of H3K27Ac status, whereas, at Bach1 co-bound regions, MafF-bound FP depth was significantly increased by both GEM treatment and PRMT1-KD regardless of H3K27Ac status (Figure 7B). Interestingly, while Prmt1-KD dramatically enhanced GEM-induced increase in Bach1 overall signals at both H3K27Ac+ and H3K27Ac− sites, Bach1 FP depths were only elevated at H3K27Ac− sites (Figure 7B).

Our data thus support the following working model: GEM induces recruitment of Bach1 to genomic loci pre-bound by MafF, which then augments the binding affinity of MafF at these sites. Subsequently, depending on the configuration of the Bach1/MafF complexes, the switch from MafF homodimers to Bach1/MafF hetero-oligomeric complexes leads either to further transcription suppression or activation. Prmt1 disrupts this process, limiting GEM-induced assembly of Bach1/MafF transcriptional complexes on the chromatin by inhibiting the MafF-Bach1 interaction and thereby promoting the acquisition of GEM resistance.

DISCUSSION

Utilizing Cut&Tag, we demonstrated a prominent role for epigenetic reprogramming in acquiring GEM resistance in PDAC. We further showed that epigenetic enzyme PRMT1 promotes acquired resistance to chemotherapy through its arginine methyltransferase activity, and the relative expression of PRMT1 signature genes correlates with survival of patients with PDAC and segregates GEM-resistant and -sensitive PDXs. One of the type I PRMT inhibitors used in our study, GSK3368715, has been tested in a phase I clinical trial of solid tumors and diffused large B cell lymphoma (NCT03666988). Although the trial was terminated early due to unfavorable benefit/risk assessment, the drug exhibited a very tolerable toxicity profile when administered at lower doses. Our findings that partial inhibition of PRMT1 activity either via shRNA or small-molecule inhibitor at a dose minimally affecting cell growth as a single agent strongly sensitizes PDAC cells to multiple chemo drugs provide a strong rationale for exploring combinations of US Food and Drug Administration (FDA)-approved chemo regiments with a low-dose PRMT1 inhibitor in patients of PDAC.

A major challenge for analyzing chromatin accessibility data is pinpointing TFs that drive the epigenetic and transcriptional changes. Motif enrichment analysis is commonly used to predict TF binding at CREs. However, most existing methods do not take into account that CREs contribute vastly differently to the transcription regulation of individual genes, depending on their activities and physical proximities to TSS. In this study, we devised a regulatory-potential model to predict TFs with a high influence by accounting for both distance and H3K27Ac signal of each TF-binding site proximal to each differential TSS. WB analysis confirmed that our improved motif enrichment method was highly effective

Author Manuscript Author Manuscript Author Manuscript Author Manuscript

in identifying TFs that were recruited to chromatin following GEM treatment in a PRMT1-dependent manner. Notably, among the top enriched TFs identified by our method, GLI1 and Smad2/3 have been shown by other studies to be directly or indirectly regulated by PRMT1.[60–62] Concordance with these existing studies underscores the effectiveness of our method in nominating key TFs involved in epigenetic reprogramming.

Through IF, WB, and Cut&Tag analysis, we demonstrated that GEM induced dynamic recruitment of MAFF/BACH1 complexes to the chromatin, a process that is modulated by PRMT1. We showed that CRISPR-mediated KO of MAFF dramatically increased GEM resistance in PDAC cells overwriting the effects of PRMT1 inhibitors, and that predicted MAFF/BACH1-regulated genes, similar to the PRMT1 signature genes, were able to segregate GEM-resistant PDXs from GEM-sensitive PDXs. Although the BACH1/MAFF complexes are involved in the regulation of multiple cellular processes, very limited chromatin profiling has been conducted for either BACH1 or MAFF. Our Cut&Tag analysis of BACH1 and MAFF provided detailed mapping of the chromatin-binding dynamics of endogenous BACH1 and MAFF at steady state and during different stages of GEM response. Our analysis revealed minimal BACH1 chromatin occupancy and low-affinity MAFF binding to its canonical motifs (probably as homodimers) in untreated PDAC cells. GEM treatment induced *de novo* gain in both MAFF and BACH1 binding across the genome. Notably, the progressive increase in BACH1 occupancy occurred primarily at sites pre-bound by MAFF, indicating gradual displacement of the MAFF homodimers with the BACH1/MAFF hetero-oligomeric complexes at these sites. Footprint analysis showed that GEM-induced gain in binding affinity of the BACH1/MAFF complex at H3K27Ac− sites was driven largely by BACH1 making direct contact with DNA, whereas MAFF remained the primary anchor of the BACH1/MAFF complex at H3K27Ac+ sites. Additional studies will be necessary to determine what causes the differential binding affinities between BACH1 and MAFF at different genomic loci and how the binding conformation of the BACH1/MAFF complex dictates their roles as transcription suppressors or activators.

Limitations of the study

Our conclusions that the PRMT1-MAFF/BACH1 signaling axis is a key regulator of chemoresistance and low-dose PRMT1 inhibitors may be used as adjuvant to the current chemotherapy regimen for treatment of advanced PDAC are limited by our lack of full understanding of the functional interactions among these proteins. As we did not detect any direct ADMA modifications of MAFF or BACH1, it is most likely that PRMT1 indirectly regulates the formation of MAFF/BACH1 complex and its chromatin recruitment. However, it remains unknown what factors in conjunction with PRMT1 modulate MAFF/BACH1 chromatin binding in response to GEM treatment. Our mechanistic study focused primarily on gemcitabine and did not investigate in depth what roles MAFF and BACH1 play in response to other chemo treatments. We also did not explore how PRMT1 influences the chromatin binding of other potentially relevant TFs. All of these questions will warrant further investigation to gain a full understanding of mechanisms of acquired chemoresistance.

Author Manuscript Author Manuscript Author Manuscript Author Manuscript

STAR★METHODS

RESOURCE AVAILABILITY

Lead contact—Further information and requests for resources and reagents should be directed to and will be fulfilled by the lead contact, Chunling Yi (cy232@georgetown.edu).

Materials availability—This study did not generate any new unique reagents.

Data and code availability

- Cut&Tag sequencing data have been deposited to NCBI Gene Expression Omnibus (GEO) database and are publicly available as of the date of publication with accession code GSE227129.
- All software used in the study are listed in the key resources table. Raw codes are available upon request.
- Any additional information required to reanalyze the data reported in this paper is available from the lead contact upon request.

EXPERIMENTAL MODEL AND STUDY PARTICIPANT DETAILS

Mice—All animal studies were conducted in compliance with ethical regulations according to protocol #2016–1192 approved by the Institutional Animal Care and Use Committee (IACUC) at Georgetown University. Two mouse strains were used: C57BL/6J (immunocompetent) and NOD.Cg-Prkdcscid/J (immunocompromised). Mice were all males, 8–10 weeks old at the beginning of the experiment. Littermates were randomly assigned to experimental groups. Mice bearing mT4 tumors were fed a Doxycycline-infused diet; all other mice received normal food.

Cell lines—Panc1 (female), MiaPaCa2 (male), and AsPC1 (female) cells were obtained from ATCC and mT4 (murine) cells were obtained from the Tuverson lab.[9] These cells were maintained in DMEM containing 1mM glucose, 10% fetal bovine serum (FBS) and 1% penicillin/streptomycin. HPAFII (male) and CAPAN-1 (male) cells obtained from ATCC were maintained in RPMI1640 containing 1mM glucose, 20% FBS and penicillin/streptomycin. Cell lines were not authenticated. Unless indicated otherwise, all cells carrying inducible shRNAs were pre-treated for at least 2 days with 4 μg/mL Dox prior to beginning an experiment. Unless indicated otherwise, 15nM GEM was used to treat mT4 cells, and 12nM GEM was used to treat human PDAC cells in all the experiments. 500nM MS023 and 100nM GSK3368715 were used to treat all PDAC lines unless noted otherwise. 5uM 5-FU and 8nM Paclitaxel were used to treat mT4 cells in the fractionation experiment. All cells were maintained in incubators at 37°C.

METHOD DETAILS

Subcutaneous tumor studies—5×10^4 parental or Doxycycline-inducible Prmt1 shRNA-expressing (shPrmt1) mT4 cells or 2×10^6 AsPC1 cells were subcutaneously injected into the left and right flanks of 8–10-week-old C57BL/6J and NOD.Cg-Prkdcscid/J mice respectively. Tumor dimensions were monitored every two

Author Manuscript Author Manuscript Author Manuscript Author Manuscript

days with caliper and tumor volume was calculated according to the formula: $Volume(mm^3) = Length(mm^2) * Width(mm^2) * (Length + Width)/2$. Once tumor volume reached ≥100 mm^3, mice bearing mT4 tumors were switched to a Doxycycline-infused food diet and 50 mg/kg Gemcitabine or saline ($N = 5$ mice each) were administered intra-peritoneally every two days, whereas mice bearing AsPC1 tumors were randomly assigned to twice-a-week IP injections with saline, 50 mg/kg Gemcitabine, 100 mg/kg GSK3368715, or both drugs combined. Mice were euthanized once tumor burden reaches 1,500mm^3 or according to IACUC guidelines. Tumors chunks were frozen or fixed with 10% Neutral Buffered Formalin for Immunohistochemistry. Statistical analyses were performed using Prism (GraphPad, Dotmatics). two-way ANOVA repeated measure and Kaplan-Meier survival analysis were used to compare tumor growth and survival between groups respectively. Significance was determined by $p < 0.05$ and error bars on graphs indicated standard error.

Generation of stable cell lines—All lentiviral plasmids used to produce or silence protein expression: pTripz, pCW57, pLIX402, pL304, TLCv2 were purchased from Addgene. Specific shRNA and sgRNA primers sequences are detailed in key resources table.

Knock-down (KD) of protein expression was achieved by ligating shRNA primer sequence into pTripz lentiviral plasmid according to supplier's recommendation. Lentiviral TLCv2 KO plasmid was generated by ligating sgRNA primer sequence into TLCv2 backbone according to supplier's recommendation.

Gateway entry plasmid for PRMT1 and MAFF were constructed using Gateway BP Clonase II Enzyme mix and PCR-product from reverse transcribed human cDNA. Entry plasmids are recombined into Destination vector using Gateway LR Clonase II Plus according to the manufacturer's instructions.

Lentiviral vectors and indicated plasmids are transfected into 293T cells using Lipofectamine 2000 according to manufacturer's instructions. Media containing lentiviral particles is harvested at 48- and 72-h. PDAC cells are infected overnight and selected using either Puromycin (10 mg/mL), blastocidin (10 mg/mL), or hygromycin (10 mg/mL) for at least 1 week prior to experiments.

Competitive growth assays—Murine PDAC parental (RFP−) and RFP-labeled (RFP+) mT4 cells expressing a Dox-inducible Prmt1 shRNA with or without reconstitution with wild-type (WT) or an enzymatically dead mutant (E171Q) human PRMT1 were incubated in Doxycycline (1:250) for at least 2 days prior to experiment. RFP+ PDAC cells (shPrmt1, Prmt1-WT, Prmt1-E171Q) were cultured together with parental cells at a 1:1 ratio in the presence of Doxycycline (1:250). Cell mixtures were treated with vehicle control or indicated concentration of chemotherapy and submitted for flow cytometry analysis to determine RFP+/RFP− cell composition at all indicated timepoints including baseline. The cells ratio (RFP+/RFP−) at any timepoint were normalized to baseline and t test were used to determine statistical significance between experimental conditions.

Author Manuscript Author Manuscript Author Manuscript Author Manuscript

Western blotting—Cells pellet or indicated cellular fractions were lysed using urea buffer (9.5 M urea, 2% CHAPS) or RIPA buffer (50 mM Tris HCl, 150 mM NaCl, 1.0% NP-40, 0.5% SDOC, 1.0 mM EDTA, 0.1% SDS) and subjected to mild agitation or sonication to fragment DNA. Cell lysates are then centrifuged at max speed (~21,000g) for 10m to remove debris. SDS-loading buffer is added to lysate and mixtures were heated at 95°C for 10m. Samples are resolved using poly-acrylamide gel electrophoresis (National Diagnostics, AccuGel Cat# EC-849) and probed with primary and HRP-conjugated secondary antibodies detailed in key resources table.

Quantitative real-time PCR—Total cell mRNA were extracted using the RNeasy minikit (QIAGEN, Hilden, Germany) according to the manufacturer's instructions. Reverse transcription was carried out using iScript reverse transcription mix (BioRad, Groningen, Netherlands). qRT-PCR for indicated transcript was performed using Forget-Me-Not EvaGreen qPCR mastermix (Biotium, CA, US) and gene expression fold change was calculated as a unit value of $2^{-\Delta Ct} = 2^{-[Ct(Ctrl)) - Ct(Gene\ of\ Interest)]]}$. Expression was normalized using GAPDH and MAPK3 as total mRNA control.

Co-immunoprecipitation—Cells were harvested and washed 1X with ice-cold PBS and centrifuged at 800g. Cell pellets are resuspended in hypotonic buffer (20mM HEPES, 20% glycerol, 10mM NaCl, 1.5mM MgCl2, 0.2mM EDTA, 0.1% NP-40, supplemented with 1mM DTT, Protease inhibitor, and 1mM Na3VO4) and pipetted up and down 5X within 10m on ice. Cell lysates are centrifuged at 1,200g for 5m at 4C and resuspended again in hypotonic buffer for 10m on ice with occasional mixing. Following membrane lysis, cell lysates are centrifuged at 1,500g for 5m at 4C to obtain nuclear pellets.

Nuclear pellets are resuspended in RIPA buffer (50 mM Tris HCl, 150 mM NaCl, 1.0% NP-40, 0.5% SDOC, 1.0 mM EDTA, 0.1% SDS) supplemented with proteinase inhibitor (PI) and Na3VO4 by pipetting for 30 m at 4C. Nuclear lysates are then sonicated for 10m (30s ON, 30s OFF), followed by centrifugation at max speed (~21,000g) for 10 m at 4C. Samples are normalized using BCA reagents (Pierce BCA Protein Assay cat# 23221) and subjected to primary antibodies or IP-beads incubation.

α-Protein-G Agarose beads (Millipore, Protein A Agarose cat# 16–201) or α-HA affinity Gel (Sigma Aldrich, EZview Red anti-HA gel cat #E6779) are washed 5X in RIPA buffer and aliquoted into each normalized protein sample for immuno-precipitation (IP) overnight at 4C. IP samples are centrifuged the next day at ~12,000g to collect IP beads. Beads are washed at least 4X with RIPA buffer and drained with $27^{1/2}$G needles. SDS loading buffer is added to samples and mixtures are prepared for western blotting as indicated.

Immunofluorescence—All antibodies used for IF were listed in key resources table. Paraformaldehyde-fixed murine and human PDAC cells were washed 3X with PBS at RT and permeabilized in 0.1% Triton X-100 PBS for 3m, followed by incubation with primary antibody for at least 1 h at 4C. cells were subsequently washed 5X with 0.1% Triton X-100 PBS and subjected to fluorescein-conjugated secondary antibodies for 30 m at RT in the dark. Cells are washed 5X with PBS at RT and mounted using mounting solution containing Hoechst-33342. Confocal fluorescent images were obtained by a Zeiss LSM 510 Meta

Author Manuscript Author Manuscript Author Manuscript Author Manuscript

confocal microscope (Jena, Germany) and processed with ImageJ software (Bethesda, MD, USA). Nuclear mean fluorescent intensity (MFI) was measured using Hoechst-33342 signal as nuclear boundary.

Apoptosis and cell cycle analysis—mT4 parental and mT4 cell expressing inducible Prmt1 shRNA were pre-treated with Doxycycline (1:250) for at least 2 days prior to treatment with GEM or vehicle control for indicated duration. ***For Apoptosis procedure***, cells were washed 1X with PBS and trypsinized at RT (Thermo Fisher cat# 25200056). Live cells were centrifuged at 2000rpm for 5m at RT. 100uL Annexin V binding buffer, 4uL of Annexin FITC, and 4uL of PI were added to cell pellets before 15m incubation in the dark. After incubation, 300uL of Annexin V binding buffer were added and samples submitted for flow cytometry. ***For cell cycle analysis***, cells were washed 1X with ice-cold PBS, trypsinized (Thermo Fisher cat# 25200056) and centrifuged at 800g for 5m to obtain cell pellets. Samples were carefully resuspended in 25% pre-chilled ethanol, centrifuged at 800g for 5m and resuspended again at 75% pre-chilled ethanol before storage at −20C. Ethanol-fixed cells were centrifuged at 2000rpm for 5m at RT and washed with 2mL of ice-cold PBS. 500uL of 0.05 mg/mL PI solution in 0.1% Triton X-100 buffer +0.001% (v/v) RNAase were mixed into cell pellets before 30m incubation in the dark. Apoptosis and cell cycle analysis were determined using Flow cytometry. Statistical analysis were carried out using FCS Express (*De Novo* software, Dotmatics).

Epigenetic inhibitor screen—Murine and human PDAC cells were seeded onto 48-well plates and treated with vehicle control (Dmso) or epigenetic inhibitors (Epi) in the absence (−GEM) or presence of GEM (+GEM). −GEM and +GEM PDAC cells were fixed with 1% Paraformaldehyde (PFD) and stained with 0.1% (w/v) Crystal Violet in 10% Ethanol at day 4 and day 10 respectively. Crystal violet-stained samples were read for absorbance at 590nm using a plate reader. Epi-treated samples were normalized to Dmso-treated samples to determine the effect of Epi in the presence or absence of GEM. Statistical significance was calculated using Prism. All epigenetic inhibitors used are listed in key resources table.

Colony formation assay—1,000 mT4 or MiaPaca2 cells were seeded onto 10cm or 6cm plates. Once stabilized (~10 cells/colony), cells were treated with indicated concentration of GEM and media is changed every two days. At day 14, cells were washed with ice-cold PBS, fixed with 1% Paraformaldehyde (PFD) and stained with 0.1% (w/v) of Crystal Violet in 10% Ethanol. Image analysis is performed with ImageJ (Bethesda, MD, USA). Statistical analysis is carried out using Prism (Graphpad, Dotmatics).

Subcellular fractionations—Cells were washed 1X with ice-cold PBS, scraped and centrifuged at 800g for 5m (4C) to obtain cell pellets. Pellets were resuspended in hypotonic buffer (20mM HEPES, 20% glycerol, 10mM NaCl, 1.5mM MgCl2, 0.2mM EDTA, 0.1% NP-40, supplemented with 1mM DTT, Protease inhibitor, and 1mM Na3VO4) and incubated on ice for 10m with frequent pipetting. Lysates were centrifuged at 1,200g for 5m at 4C and supernatant collected as cytoplasmic fractions. Pellets were resuspended again in excess hypotonic buffer for 10m on ice with occasional mixing. A portion of the lysates were aliquoted and saved as total nuclear fraction. The remaining nuclear fractions were

Author Manuscript Author Manuscript Author Manuscript Author Manuscript

centrifuged at 1,200g for 5m at 4C. Following aspiration, nuclear fractions were resuspended with ice-cold E2 buffer (10mM Tris-HCl, 200mM NaCl, 1mM EDTA, 0.5mM EGTA, supplemented with Protease inhibitor cocktail, 1mM Na3VO4) for 10m on ice with frequent pipetting. Nuclear lysates were centrifuged at 1,200g for 5m at 4C. Supernatants were collected as soluble nuclear fraction and pellets were further resuspended in excess E2 buffer for 10m on ice with occasional mixing. After centrifugation at 1,500g for 5m at 4C, pellets were collected as chromatin fraction that can be stored at −80C for further processing. Finally, the chromatin pellets were resuspended with E3 buffer (500mM Tris-HCl, 500mM NaCl, 1mM MgCl2, supplemented with Protease inhibitor cocktail and 10ug/mL DNAse). Chromatin lysates are passed through $27^{1/2}$G needles 5X and subjected to sonication for 10m (30s ON, 30s OFF), and let incubate on rotator for 20 m at 4C to create chromatin protein fraction. All protein fractions were centrifuged at >16,000g for 10 m at 4C to remove debris and transferred into new 1.5mL tubes. SDS-loading buffer was added to each cellular fraction and lysates were incubated at 90C for 10m. Protein lysates were quantified and normalized using BCA reagent for further analysis.

Cut&Tag—All antibodies used for Cut&Tag were listed in key resources table. Cut&Tag was carried out according to the bench top Cut&Tag V.3 with minor modifications. PDAC cells were harvested using cell stripper (Thermo Fishers), counted and centrifuged for 3 min at 800×*g* at room temperature. Aliquots of 250,000 cells per sample per antibody were washed twice in 100 μL per sample of Wash Buffer (20 mM HEPES pH 7.5, 150 mM NaCl, 0.5 mM Spermidine, 1× Protease inhibitor cocktail) by gentle pipetting. Concanavalin A (ConA) coated magnetic beads (Bangs Laboratories, Fishers, IN) were washed twice with ConA Binding Buffer (20 mM HEPES pH7.5, 10 mM KCl, 1 mM $CaCl_2$, 1 mM $MnCl_2$) and 10 μL of activated beads were added per sample and incubated at RT for 15 min on rotator. ConA bead-bound cells were placed on the magnetic stand and the unbound supernatant was removed. ConA bead-bound cells were resuspended in ice-cold 100 μL Dig-wash Buffer (20 mM HEPES pH 7.5, 150 mM NaCl; 0.5 mM Spermidine, 1× Protease inhibitor cocktail, 0.05% Digitonin) containing 2 mM EDTA and diluted primary antibody indicated on key resources table. Primary antibody incubation was performed on a rotating platform for 2 h at room temperature (RT). The primary antibody was removed by placing the tube on the magnet stand to clear and pulling off all of the liquid. Guinea Pig anti-Rabbit IgG secondary antibody was diluted 1:100 in 100 μL of Dig-Wash buffer and cells were incubated at RT for 1 h. Cells were washed using the magnet stand 5 times in 150 μL Dig-Wash buffer to remove unbound antibodies. After removing the liquid on the magnet stand, 100 μL protein A (pA)-Tn5 adapter complex diluted 1:100 in Dig-300 Buffer (0.05% Digitonin, 20 mM HEPES, pH 7.5, 300 mM NaCl, 0.5 mM Spermidine, 1× Protease inhibitor cocktail) was added to the cells with gentle vortexing and incubated at RT for 1 h pA-Tn5 adaptor complex was prepared by mixing pA-Tn5 (Addgene) fusion protein with preannealed mosaic end-adaptor A and -adaptor B and incubation for 1 h at RT. Cells were washed 5 times in 150 μL Dig-300 Buffer to remove unbound pA-Tn5 protein. Cells were resuspended in 200 μL Tagmentation buffer (10 mM $MgCl_2$ in Dig-300 Buffer) and incubated at 37°C for 1 h. To stop tagmentation, 6.67 μL of 0.5 M EDTA, 2 μL of 10% SDS and 1.67 μL of 20 mg/mL Proteinase K was added to sample, and incubated at 50 °C for 30 min, and then at 37 °C overnight. To extract the DNA, 200 μL PCI were added and

Author Manuscript Author Manuscript Author Manuscript Author Manuscript

mixed with vortexing. 200 μL vacuum grease was added to separate layers of protein and DNA, and tubes were centrifuged for 3 min at RT 16,000×g. 200 μL Chloroform was added and inverted 10 times, and tubes were centrifuged for 3 min at RT 16,000×g. The aqueous layer was transferred to new tube containing 500 μL ice-cold 100% ethanol and centrifuged for 15 min at 4 °C 16,000×g. The pellet was rinsed with 100% ethanol, centrifuged for 2 min at 4 °C 16,000×g. After the liquid was aspirated, the pellet was dissolved in 30 μL 10 mM Tris-HCl pH8, 1 mM EDTA containing RNaseA. PCR was performed with NEBNext HiFi 2x PCR Master mix (NEB, Ipswich, MA), unique i7 barcode primer, and Universal i5 primer. To extract the DNA, 0.4 volume Mag-Bind TotalPure NGS beads (Omega Bio Tech, Norcross, GA) were added to each tube with vortexing, quickly spun and held 10 min. Tubes were placed on a magnet stand to clear, then the liquid was transferred to new tube. 0.7 volume volume Mag-Bind TotalPure NGS beads were added to each tube with vortexing, quickly spun and held 10 min. Tubes were placed on a magnet stand to clear, then the liquid was carefully withdrawn. Without disturbing the beads, beads were washed twice in 200 μL 80% ethanol. After allowing to dry ~5 min, 30 μL of 10 mM Tris pH 8 was added, the tubes were vortexed, quickly spun and allowed to sit for 5 min at 37 °C. Tubes were placed on a magnet stand and the liquid was withdrawn to a fresh tube.

Barcoded Cut&Tag libraries were prepared using NebNext High-Fidelity 2X PCR Master Mix (Ipswich, Massachusetts, USA) with Nextera i7 and i5 dual index primers, purified with Mag-Bind TotalPure NGS beads, quantified via qPCR using the KAPA Library Quantification Kit. Pooled libraries were sequenced on the Illumina High-seq platform (Read 1: 150 cycles, Index 1: 8 cycles, Index 2: 8 cycles, Read 2: 150 cycles).

QUANTIFICATION AND STATISTICAL ANALYSIS

Cut&Tag data preprocessing—Raw sequencing fastq files were assessed for quality control using FastQC and trimmed to remove adaptor sequences using cutadapt.[72] Quality reads were mapped to Ecoli and mouse genome (mm10) sequentially using Bowtie2[73] with options -very-sensitivelocal -nomixed -dovetail -phred33 -X 1000 -interleaved. Duplicated reads and blacklisted regions were filtered out using picard tools (https://github.com/broadinstitute/picard.git) and bedtools.[74] HOMER suite[67] was used to query counts in mapped.bam files to generate TagDirectory for each experiment with options -sspe; which were then used to normalize all samples within each experiment using “csaw”[75] R package with the following parameters minq = 20, max.frag = 800, pe = both, bin = TRUE, width = 10000. Processed reads were then annotated to provide normalized count matrix with annotation for each individual experiment using findPeaks.pl and annotatePeaks.pl from HOMER suite respectively with the following parameters: -style histone -localSize 500000 -F 0 -L 0 -C 0 -size 150 -minDist 2500 -fdr 0.00001 for histones and -style factor -L 15 -localSize 150000 -fdr 0.00001 for transcription factors. Finally, bigwig visualization track files were generated using makeUCSCfile with options: -bigWig –norm {scaling factor}.

Fuzzy C-mean clustering—H3K27Ac signal from Cut&Tag of murine PDAC cells treated with GEM was normalized across all timepoints (D0,2,4,6,8,10) and filtered for peaks with at least one timepoint having normalized signal count ≥10. Log2(FC), Poisson distribution *p*p-value, and rank difference were computed for H3K27Ac signal from each

Author Manuscript Author Manuscript Author Manuscript Author Manuscript

timepoint compared to baseline (D0) across all detected peaks. H3K27Ac Peaks that exhibited significant change in at least one sample compared to baseline (|FC|≥2; *p*p-value≤0.05; ΔRank≥500) were selected for further fuzzy c-mean clustering analysis[12] (k = 3) using R package "TCseq" to identify major patterns of change. Following unsupervised c-mean clustering, counts were queried within a +/−3kb region surrounding differentially expressed H3K27Ac peaks based on Cut&Tag experiment's normalized bigwig files using the command normalizeToMatrix with options (mean_mode = "w0", w = 20). Tornado plots were generated from queried counts for each timepoint using R package "EnrichedHeatmap".[65]

GSEA & GREAT analysis—Differentially expressed TSS were determined based on distance (≤500bp) to the nearest differential H3K27Ac peaks (|FC|≥2; *p*p-value≤0.05; ΔRank≥500) for each GEM treatment timepoints (D0,2,4,6,8,10) as determined by Cut&Tag. For each indicated timepoint, GSEA[15,16] were performed for both up- and down-regulated TSSs. −Log10 (adjusted *p*p-value) were computed for the most enriched genesets and plotted using R package "pHeatmap". For GREAT analysis, peaks assigned to each of the major three clusters from Fuzzy C-mean Clustering was analyzed using the rGREAT package under default setting.[76]

Motif enrichment—Distance Signal (DS) score is used to predict TFs that are regulated by Prmt1 using a regulatory-potential model. Each TF is assigned a DS score based on the H3K27Ac signal enrichment at that TF's binding motif and the distance of each motif to the nearest differentially expressed TSS using the following equation:

$$\mathrm{DS}\ \ Score\ \ = \sum_{1}^{ij} Log\ \ 10(Sj)/(1 + Dij)$$

In which, DS score is calculated as the sum of log10 transformed signals (**S**) of differential H3K27Ac CRE peaks that overlap the canonical motif of the $\mathbf{TF} - \boldsymbol{j}$ divided by their distances (D) to adjacent differential H3K27Ac TSS peaks. $\mathbf{S}\boldsymbol{j}$ represents the signal of a given differential H3K27Ac CRE peak that overlaps the motif of a given $\mathbf{TF} - \boldsymbol{j}$; $\mathbf{D} - \boldsymbol{i}, \boldsymbol{j}$ represent the distance between a given differential H3K27Ac CRE peak that overlaps the motif of $\mathbf{TF} - \boldsymbol{j}$ and a given adjacent differential H3K27Ac TSS peak $\boldsymbol{i}$.

Utilizing H3K27Ac Cut&Tag of murine PDAC parental and Prmt1 shRNA-expressing cells in absence or presence of GEM, we detected 2,356 Prmt1-regulated TSSs that are proximal to differential H3K27Ac peaks between parental and Prmt1 KD PDAC cells in presence of GEM (|FC|≥2; *p*p-value≤0.05; ΔRank≥500). Curated annotation of TF motifs that have detectable H3K27Ac signal at their promoters was downloaded from https://resources.altius.org/~jvierstra/. Using the equation indicated above, we computed and ranked the DS score for TFs against 2,356 Prmt1-regulated TSSs. Calculated DS Score were plotted using R package "EnrichedHeatmap".

HSV transformation—Differential peak signal of H3K27Ac, MAFF, or BACH1 (|FC|≥2; *p*p-value≤0.05; ΔRank≥500) determined by Cut&Tag among murine PDAC parental treated

Author Manuscript Author Manuscript Author Manuscript Author Manuscript

with vehicle control (D0), GEM (D1) or shPrmt1-expressing PDAC cells treated with GEM (D2) were used to compute HSV values as follows:

$$V = \sum_{i=1}^{n} \max(D0[i], D1[i], D2[i])$$

$$S = \sum_{i=1}^{n} 1 - \min\frac{(D0[i], D1[i], D2[i])}{V[i]}$$

$$H = \sum_{i=1}^{n} \left(\frac{(D0[i] + D1[i] - D2[i] - V[i])}{S[i] \times V[i]} + 2\right) \times sign(D1[i] - D0[i]) \times 60$$

In Which, V is Value, S is saturation, H is Hue, and n is the number of differentially expressed peaks detected. These equations allow transformation of sequential data (D0-D1-D2) into distinct groups of angular values which represents chromatin peak signal profiles (i.e., High-low-high) that can be represented on a circular plot (Figure 4A). H is calculated as the angular position of a single chromatin peak signal on the polar plot (0–360°) whereas, the color represents the normalized signal profile of D0-D1-D2 (i.e., red; H = 0° stands for no change in chromatin signal from D0→D1 and increase in chromatin signal from D1→D2). MaxLog was calculated as Log10 of maximal signal difference for each peak between any condition. HSV plot was generated using R package ggplot2.

MDS and PCA analysis—Differential chromatin peak signal (Cut&Tag) and transcript reads (RNAseq) were used as input to compute dissimilarity/similarity distance matrix using plotMDS (R package “limma”[69]) or prcomp (R package “stats”). MDS and PCA plots were generated with R package ggplot2.

TOBIAS footprinting analysis—We utilized R package “TOBIAS”[59] with default settings for detection of genomic footprint. The “JASPAR2022_CORE_vertebrates_non-42 redundant_pfms_jaspar.txt” file was downloaded from “https://jaspar.genereg.net/downloads/”. H3K27Ac, MAFF, and BACH1 Cut&Tag.bam files were corrected for bias using ATACcorrect module to produce bias-corrected bigwig files. FootprintingScores module is then used to quantify both footprint “accessibility” and “depth”, defined as signal above corrected baseline and total depth from peak to trough respectively. ScoreBeds module were used to score footprints quality. Finally, module BinDetect and plotAggregate were used to compare specific TF motifs from JASPAR across samples and plot footprint aggregates over genomic regions of interest.

TCGA & human PDXs RNA-seq analysis—TCGA human pancreatic ductal cancer (PAAD) RNA sequencing & clinical data was downloaded from (https://portal.gdc.cancer.gov/repository). Fpkm normalized count matrix was filtered for transcripts

Author Manuscript Author Manuscript Author Manuscript Author Manuscript

that have fpkm≥2 in at least 50% of total patient samples and have standard deviation in the top 90th percentile of transcripts.

Human PDXs RNA sequencing fastq files were downloaded from SRP303224.[17] Raw data preprocessing and mapping to human genome was performed using STAR with options –outSAMtype BAM SortedByCoordinate –readFilesCommand zcat –genomeLoad LoadAndKeep –limitBAMsortRAM 30000000000. TagDirectory for each sample was generated using HOMER suite with options -sspe and bigwig files were created using makeUCSCfiles. HOMER suite command AnalyzeRepeats.pl was used to generate raw and rpkm count matrices for all patients' samples with the following options -strand both -condenseGenes -count exons. PCA analysis was carried out on rpkm normalized counts to remove anomalous samples. Raw counts were used as input for Deseq2 normalization, enrichment, and annotation with the following design ~ condition + condition:GemSensitivity or ~GemSensitivity + GemSensitivity:condition.[77] Normalized counts were filtered for genes with count>0 in at least 50% of samples. Kaplan-Meier survival analysis on both TCGA and human PDXs clinical data was performed with R package "survival" and "survminer".

Supplementary Material

Refer to Web version on PubMed Central for supplementary material.

ACKNOWLEDGMENTS

We thank Dr. Alec McIntosh for critical comments of the manuscript. We appreciate the technical assistance from Rachel Nas, the Flow Cytometry and Cell Sorting Shared Resource (FCSR), and Microscopy & Imaging Shared Resource (MISR) at Lombardi Cancer Center Shared Resources. We thank the husbandry staff and technicians of the Division of Comparative Medicine (DCM) at Georgetown University for support in our animal studies. This project is supported by R01CA252223 (NIH), R21CA258153 (NIH), and P30CA051008 (NIH). C.D.K.N. has been supported by NIH T32CA009686 and F31CA247417.

REFERENCES

1. Siegel RL, Miller KD, Fuchs HE, and Jemal A (2021). Cancer Statistics, 2021. CA. Cancer J. Clin. 71, 7–33. 10.3322/CAAC.21654. [PubMed: 33433946]
2. von Hoff DD, Ervin T, Arena FP, Chiorean EG, Infante J, Moore M, Seay T, Tjulandin SA, Wee Ma W, Saleh N, et al. (2013). Increased Survival in Pancreatic Cancer with nab-Paclitaxel plus Gemcitabine. NEJM.org. N. Engl. J. Med. 18, 1691–1703. 10.1056/NEJMoa1304369.
3. Tsujimoto A, Sudo K, Nakamura K, Kita E, Hara R, Takayama W, Ishii H, and Yamaguchi T (2019). Gemcitabine plus nab-paclitaxel for locally advanced or borderline resectable pancreatic cancer. Sci. Rep, 16187–16188. 10.1038/s41598-019-52486-x. [PubMed: 31700023]
4. Miranda Furtado CL, Dos Santos Luciano MC, Silva Santos RD, Furtado GP, Moraes MO, and Pessoa C (2019). Epidrugs: targeting epigenetic marks in cancer treatment. Epigenetics 14, 1164–1176. 10.1080/15592294.2019.1640546. [PubMed: 31282279]
5. Barth TK, and Imhof A (2010). Fast signals and slow marks: the dynamics of histone modifications. Trends Biochem. Sci. 35, 618–626. 10.1016/J.TIBS.2010.05.006. [PubMed: 20685123]
6. Liau BB, Sievers C, Donohue LK, Gillespie SM, Flavahan WA, Miller TE, Venteicher AS, Hebert CH, Carey CD, Rodig SJ, et al. (2017). Adaptive chromatin remodeling drives glioblastoma stem cell plasticity and drug tolerance. Cell Stem Cell 20, 233–246.e7. 10.1016/J.STEM.2016.11.003. [PubMed: 27989769]

Author Manuscript Author Manuscript Author Manuscript Author Manuscript

7. Sharma S.v., Lee DY, Li B, Quinlan MP, Takahashi F, Maheswaran S, McDermott U, Azizian N, Zou L, Fischbach MA, et al. (2010). A chromatin-mediated reversible drug tolerant state in cancer cell subpopulations. Cell 141, 69–80. 10.1016/J.CELL.2010.02.027. [PubMed: 20371346]
8. Macchini M, Peretti U, Orsi G, Zanon S, Mazza E, Valente MM, Tamburrino D, Belfiori G, Rossi G, Testoni SGG, et al. (2021). Exploring chemotherapy holiday and drugs re-challenge in advanced pancreatic cancer patients. Cancer Chemother. Pharmacol. 87, 95–101. 10.1007/S00280-020-04190-1/FIGURES/1. [PubMed: 33159215]
9. Boj SF, Hwang CI, Baker LA, Chio IIC, Engle DD, Corbo V, Jager M, Ponz-Sarvise M, Tiriac H, Spector MS, et al. (2015). Organoid Models of Human and Mouse Ductal Pancreatic Cancer. Cell 160, 324–338. 10.1016/J.CELL.2014.12.021. [PubMed: 25557080]
10. Kaya-Okur HS, Wu SJ, Codomo CA, Pledger ES, Bryson TD, Henikoff JG, Ahmad K, and Henikoff S (2019). CUT& Tag for efficient epigenomic profiling of small samples and single cells. Nat. Commun. 10, 1930. 10.1038/s41467-019-09982-5. [PubMed: 31036827]
11. Robinson MD, McCarthy DJ, and Smyth GK (2010). edgeR: a Bioconductor package for differential expression analysis of digital gene expression data. Bioinformatics 26, 139–140. 10.1093/BIOINFORMATICS/BTP616. [PubMed: 19910308]
12. Bezdek JC, Ehrlich R, and Full W (1984). FCM: The fuzzy c-means clustering algorithm. Comput. Geosci. 10, 191–203. 10.1016/0098-3004(84)90020-7.
13. Mclean CY, Bristor D, Hiller M, Clarke SL, Schaar BT, Lowe CB, Wenger AM, and Bejerano G (2010). An Alysis GREAT improves functional interpretation of cis-regulatory regions. Nat. Biotechnol. 28, 495–501. 10.1038/nbt.1630. [PubMed: 20436461]
14. Jenuwein T, and Allis CD (2001). Translating the histone code. Science (1979) 293, 1074–1080. 10.1126/SCIENCE.1063127/ASSET/FCD15CEA-ECDC-41AF-AE32-FEDCEA8620CC/ASSETS/GRAPHIC/SE3119652003.JPEG.
15. Subramanian A, Tamayo P, Mootha VK, Mukherjee S, Ebert BL, Gillette MA, Paulovich A, Pomeroy SL, Golub TR, Lander ES, and Mesirov JP (2005). Gene set enrichment analysis: A knowledge-based approach for interpreting genome-wide expression profiles. Proc. Natl. Acad. Sci. USA 102, 15545–15550. 10.1073/PNAS.0506580102/SUPPL_FILE/06580FIG7.JPG. [PubMed: 16199517]
16. Mootha VK, Lindgren CM, Eriksson KF, Subramanian A, Sihag S, Lehar J, Puigserver P, Carlsson E, Ridderstråle M, Laurila E, et al. (2003). PGC-1α-responsive genes involved in oxidative phosphorylation are coordinately downregulated in human diabetes. Nat. Genet. 34, 267–273. 10.1038/ng1180. [PubMed: 12808457]
17. Yang G, Guan W, Cao Z, Guo W, Xiong G, Zhao F, Feng M, Qiu J, Liu Y, Zhang MQ, et al. (2021). Integrative genomic analysis of gemcitabine resistance in pancreatic cancer by patient-derived xenograft models. Clin. Cancer Res. 27, 3383–3396. 10.1158/1078-0432.CCR-19-3975/15431/AM/INTEGRATIVE-GENOMIC-ANALYSIS-OF-GEMCITABINE. [PubMed: 33674273]
18. Zurita-Lopez CI, Sandberg T, Kelly R, and Clarke SG (2012). Human protein arginine methyltransferase 7 (PRMT7) is a type III enzyme forming u-N G-monomethylated arginine residues. J. Biol. Chem. 287, 7859–7870. 10.1074/jbc.M111.336271. [PubMed: 22241471]
19. Ougolkov A.v., Bilim VN, and Billadeau DD (2008). Regulation of pancreatic tumor cell proliferation and chemoresistance by the histone methyltransferase enhancer of zeste homologue 2. Clin. Cancer Res. 14, 6790–6796. 10.1158/1078-0432.CCR-08-1013. [PubMed: 18980972]
20. Wolf SS (2009). The protein arginine methyltransferase family: An update about function, new perspectives and the physiological role in humans. Cell. Mol. Life Sci. 66, 2109–2121. 10.1007/S00018-009-0010-X/FIGURES/3. [PubMed: 19300908]
21. Shailesh H, Zakaria ZZ, Baiocchi R, and Sif S (2018). Protein Arginine Methyltransferase 5 (PRMT5) Dysregulation in Cancer. Oncotarget 9, 36705–36718. [PubMed: 30613353]
22. Obianyo O, Causey CP, Jones JE, and Thompson PR (2011). Activity-based protein profiling of protein arginine methyltransferase 1. ACS Chem. Biol. 6, 1127–1135. 10.1021/cb2001473.
23. Vierstra J, and Stamatoyannopoulos JA (2016). Genomic footprinting. Nat. Methods, 213–221. 10.1038/nmeth.3768. [PubMed: 26914205]

Author Manuscript Author Manuscript Author Manuscript Author Manuscript

24. Fedoriw A, Rajapurkar SR, O'Brien S, Gerhart S.v., Mitchell LH, Adams ND, Rioux N, Lingaraj T, Ribich SA, Pappalardi MB, et al. (2019). Anti-tumor Activity of the Type I PRMT Inhibitor, GSK3368715, Synergizes with PRMT5 Inhibition through MTAP Loss. Cancer Cell 36, 100–114.e25. 10.1016/J.CCELL.2019.05.014. [PubMed: 31257072]
25. Mitchell LH, Drew AE, Ribich SA, Rioux N, Swinger KK, Jacques SL, Lingaraj T, Boriack-Sjodin PA, Waters NJ, Wigle TJ, et al. (2015). Aryl Pyrazoles as Potent Inhibitors of Arginine Methyltransferases: Identification of the First PRMT6 Tool Compound. ACS Med. Chem. Lett. 6, 655–659. 10.1021/ACSMEDCHEMLETT.5B00071. [PubMed: 26101569]
26. Yan L, Yan C, Qian K, Su H, Kofsky-Wofford SA, Lee WC, Zhao X, Ho MC, Ivanov I, and Zheng YG (2014). Diamidine compounds for selective inhibition of protein arginine methyltransferase 1. J. Med. Chem. 57, 2611–2622. 10.1021/JM401884Z. [PubMed: 24564570]
27. Srour N, Villarreal OD, Hardikar S, Yu Z, Preston S, Miller WH, Szewczyk MM, Barsyte-Lovejoy D, Xu H, Chen T, et al. (2022). PRMT7 ablation stimulates anti-tumor immunity and sensitizes melanoma to immune checkpoint blockade. Cell Rep. 38, 110582. 10.1016/J.CELREP.2022.110582. [PubMed: 35354055]
28. Penebre E, Kuplast KG, Majer CR, Boriak-Sjodin A, Wigle TJ, Johnston D, Rioux N, Munchhof MJ, Jin L, Jacques SL, et al. (2014). Identification of a First-In-Class PRMT5 Inhibitor with Potent in Vitro and in Vivo Activity in Preclinical Models of Mantle Cell Lymphoma. Blood 124, 438.
29. Shen Y, Szewczyk MM, Eram MS, Smil D, Kaniskan HÜ, de Freitas RF, Senisterra G, Li F, Schapira M, Brown PJ, et al. (2016). Discovery of a Potent, Selective, and Cell-Active Dual Inhibitor of Protein Arginine Methyltransferase 4 and Protein Arginine Methyltransferase 6. J. Med. Chem. 59, 9124–9139. 10.1021/ACS.JMED-CHEM.6B01033. [PubMed: 27584694]
30. Kim E, Jang J, Park JG, Kim KH, Yoon K, Yoo BC, and Cho JY (2020). Protein Arginine Methyltransferase 1 (PRMT1) Selective Inhibitor, TC-E 5003, Has Anti-Inflammatory Properties in TLR4 Signaling. Int. J. Mol. Sci. 21, 3058. 10.3390/IJMS21093058. [PubMed: 32357521]
31. Kaniskan HÜ, Szewczyk MM, Yu Z, Eram MS, Yang X, Schmidt K, Luo X, Dai M, He F, Zang I, et al. (2015). A potent, selective and cell-active allosteric inhibitor of protein arginine methyltransferase 3 (PRMT3). Angew. Chem. Int. Ed. Engl. 54, 5166–5170. 10.1002/ANIE.201412154. [PubMed: 25728001]
32. Bissinger EM, Heinke R, Spannhoff A, Eberlin A, Metzger E, Cura V, Hassenboehler P, Cavarelli J, Schüle R, Bedford MT, et al. (2011). Acyl derivatives of p-aminosulfonamides and dapsone as new inhibitors of the arginine methyltransferase hPRMT1. Bioorg. Med. Chem. 19, 3717–3731. 10.1016/J.BMC.2011.02.032. [PubMed: 21440447]
33. Eram MS, Shen Y, Szewczyk M, Wu H, Senisterra G, Li F, Butler K.v., Kaniskan HÜ, Speed BA, Dela Seña C, et al. (2016). A Potent, Selective, and Cell-Active Inhibitor of Human Type I Protein Arginine Methyltransferases. ACS Chem. Biol. 11, 772–781. 10.1021/ACSCHEMBIO.5B00839. [PubMed: 26598975]
34. Rust HL, Zurita-Lopez CI, Clarke S, and Thompson PR (2011). Mechanistic studies on transcriptional coactivator protein arginine methyltransferase 1. Biochemistry 50, 3332–3345. 10.1021/bi102022e. [PubMed: 21417440]
35. Huang S, Litt M, and Felsenfeld G (2005). Methylation of histone H4 by arginine methyltransferase PRMT1 is essential in vivo for many subsequent histone modifications. Genes Dev. 19, 1885–1893. 10.1101/GAD.1333905. [PubMed: 16103216]
36. Strahl BD, Briggs SD, Brame CJ, Caldwell JA, Koh SS, Ma H, Cook RG, Shabanowitz J, Hunt DF, Stallcup MR, and Allis CD (2001). Methylation of histone H4 at arginine 3 occurs in vivo and is mediated by the nuclear receptor coactivator PRMT1. Curr. Biol. 11, 996–1000. 10.1016/S0960-9822(01)00294-9. [PubMed: 11448779]
37. Alexanian M, Przytycki PF, Micheletti R, Padmanabhan A, Ye L, Travers JG, Gonzalez-Teran B, Silva AC, Duan Q, Ranade SS, et al. (2021). A Transcriptional Switch Governs Fibroblast Activation in Heart Disease. Nature 595, 438–443. 10.1038/S41586-021-03674-1. [PubMed: 34163071]
38. Niewiadomski P, Niedziółka SM, Markiewicz Ł, Uśpieński T, Baran B, and Chojnowska K (2019). Gli Proteins: Regulation in Development and Cancer. Cells 8, 147. 10.3390/CELLS8020147. [PubMed: 30754706]

Author Manuscript Author Manuscript Author Manuscript Author Manuscript

39. Huang Y, Nahar S, Nakagawa A, Fernandez-Barrena MG, Mertz JA, Bryant BM, Adams CE, Mino-Kenudson M, von Alt KN, Chang K, et al. (2016). Regulation of GLI underlies a role for BET bromodomains in pancreatic cancer growth and the tumor microenvironment. Clin. Cancer Res. 22, 4259–4270. 10.1158/1078-0432.CCR-15-2068. [PubMed: 27169995]
40. Nelson JK, Thin MZ, Evan T, Howell S, Wu M, Almeida B, Legrave N, Koenis DS, Koifman G, Sugimoto Y, et al. (2022). USP25 promotes pathological HIF-1-driven metabolic reprogramming and is a potential therapeutic target in pancreatic cancer. Nat. Commun. 13, 2070. 10.1038/S41467-022-29684-9. [PubMed: 35440539]
41. Gu X, Zhu Q, Tian G, Song W, Wang T, Wang A, Chen X, and Qin S (2022). KIF11 manipulates SREBP2-dependent mevalonate cross talk to promote tumor progression in pancreatic ductal adenocarcinoma. Cancer Med. 11, 3282–3295. 10.1002/CAM4.4683. [PubMed: 35619540]
42. Yang J, Zhang X, Zhang Y, Zhu D, Zhang L, Li Y, Zhu Y, Li D, and Zhou J (2016). HIF-2a promotes epithelial-mesenchymal transition through regulating Twist2 binding to the promoter of E-cadherin in pancreatic cancer. J. Exp. Clin. Cancer Res. 35, 26. 10.1186/s13046-016-0298-y.
43. Sun Y, He W, Luo M, Zhou Y, Chang G, Ren W, Wu K, Li X, Shen J, Zhao X, and Hu Y (2015). SREBP1 regulates tumorigenesis and prognosis of pancreatic cancer through targeting lipid metabolism. Tumour Biol. 36, 4133–4141. 10.1007/S13277-015-3047-5. [PubMed: 25589463]
44. Huang X, Zheng J, Li J, Che X, Tan W, Tan W, Shao M, Cheng X, Du Z, Zhao Y, et al. (2018). Functional role of BTB and CNC Homology 1 gene in pancreatic cancer and its association with survival in patients treated with gemcitabine. Theranostics 8, 3366–3379. 10.7150/THNO.23978. [PubMed: 29930735]
45. Moon EJ, Mello SS, Li CG, Chi JT, Thakkar K, Kirkland JG, Lagory EL, Lee IJ, Diep AN, Miao Y, et al. (2021). The HIF target MAFF promotes tumor invasion and metastasis through IL11 and STAT3 signaling. Nat. Commun, 4308–4318. 10.1038/s41467-021-24631-6. [PubMed: 34262028]
46. Singh P, Wig JD, and Srinivasan R (2011). The Smad family and its role in pancreatic cancer. Indian J. Cancer 48, 351–360. 10.4103/0019-509X.84939.
47. Ezrova Z, Nahacka Z, Stursa J, Werner L, Vlcak E, Kralova Viziova P, Berridge M.v., Sedlacek R, Zobalova R, Rohlena J, et al. (2021). SMAD4 loss limits the vulnerability of pancreatic cancer cells to complex I inhibition via promotion of mitophagy. Oncogene 40, 2539–2552. 10.1038/s41388-021-01726-4. [PubMed: 33686239]
48. Shen W, Xu T, Chen D, and Tan X (2019). Targeting SREBP1 chemosensitizes colorectal cancer cells to gemcitabine by caspase-7 upregulation. Bioengineered 10, 459–468. 10.1080/21655979.2019.1676485. [PubMed: 31601152]
49. Zhuang J, Shen L, Yang L, Huang X, Lu Q, Cui Y, Zheng X, Zhao X, Zhang D, Huang R, et al. (2017). TGFb1 Promotes Gemcitabine Resistance through Regulating the LncRNA-LET/NF90/miR-145 Signaling Axis in Bladder Cancer. Theranostics 7, 3053–3067. 10.7150/THNO.19542. [PubMed: 28839463]
50. Gujral TS, and Kirschner MW (2017). Hippo pathway mediates resistance to cytotoxic drugs. Proc. Natl. Acad. Sci. USA 114, E3729–E3738. 10.1073/PNAS.1703096114/SUPPL_FILE/PNAS.1703096114.SAPP.PDF. [PubMed: 28416665]
51. Kataoka K, Igarashi K, Itoh K, Fujiwara KT, Noda M, Yamamoto M, and Nishizawa M (1995). Small Maf proteins heterodimerize with Fos and may act as competitive repressors of the NF-E2 transcription factor. Mol. Cell Biol. 15, 2180–2190. 10.1128/MCB.15.4.2180. [PubMed: 7891713]
52. Kobayashi A, Ito E, Toki T, Kogame K, Takahashi S, Igarashi K, Hayashi N, and Yamamoto M (1999). Molecular cloning and functional characterization of a new Cap'n' collar family transcription factor Nrf3. J. Biol. Chem. 274, 6443–6452. 10.1074/JBC.274.10.6443. [PubMed: 10037736]
53. Johnsen Ø, Murphy P, Prydz H, and Kolstø AB (1998). Interaction of the CNC-bZIP factor TCF11/LCR-F1/Nrf1 with MafG: binding-site selection and regulation of transcription. Nucleic Acids Res. 26, 512–520. 10.1093/NAR/26.2.512. [PubMed: 9421508]
54. T O., K I., H, M., N H., H H., M N., M Y., and K I. (1996). Bach proteins belong to a novel family of BTB-basic leucine zipper transcription factors that interact with MafK and regulate transcription through the NF-E2 site. Mol. Cell Biol. 16, 6083–6095. 10.1128/MCB.16.11.6083. [PubMed: 8887638]

Author Manuscript Author Manuscript Author Manuscript Author Manuscript

55. Igarashi K, Kataoka K, Itoh K, Hayashi N, Nishizawa M, and Yamamoto M (1994). Regulation of transcription by dimerization of erythroid factor NF-E2 p45 with small Maf proteins. Nature 367, 568–572. 10.1038/367568A0. [PubMed: 8107826]
56. Blackwell TK, Bowerman B, Priess JR, and Weintraub H (1994). Formation of a monomeric DNA binding domain by Skn-1 bZIP and homeodomain elements. Science 266, 621–628. 10.1126/SCIENCE.7939715. [PubMed: 7939715]
57. Ito N, Watanabe-Matsui M, Igarashi K, and Murayama K (2009). Crystal structure of the Bach1 BTB domain and its regulation of homodimerization. Gene Cell. 14, 167–178. 10.1111/J.1365-2443.2008.01259.X.
58. Yoshida C, Tokumasu F, Hohmura KI, Bungert J, Hayashi N, Nagasawa T, Engel JD, Yamamoto M, Takeyasu K, and Igarashi K (1999). Long range interaction of cis-DNA elements mediated by architectural transcription factor Bach1. Gene Cell. 4, 643–655. 10.1046/J.1365-2443.1999.00291.X.
59. Bentsen M, Goymann P, Schultheis H, Klee K, Petrova A, Wiegandt R, Fust A, Preussner J, Kuenne C, Braun T, et al. (2020). ATAC-seq footprinting unravels kinetics of transcription factor binding during zygotic genome activation. Nat. Commun. 11, 4267–4311. 10.1038/s41467-020-18035-1. [PubMed: 32848148]
60. Katsuno Y, Qin J, Oses-Prieto J, Wang H, Jackson-Weaver O, Zhang T, Lamouille S, Wu J, Burlingame A, Xu J, et al. (2018). Arginine methylation of SMAD7 by PRMT1 in TGF-b-induced epithelial-mesenchymal transition and epithelial stem-cell generation. J. Biol. Chem. 293, 13059–137072. 10.1074/JBC.RA118.002027. [PubMed: 29907569]
61. Wu J, Chen X, Sehgal P, Zhang T, Jackson-Weaver O, Gou Y, Bautch V, Frenkel B, Sun H, and Xu J (2021). Arginine methylation of R81 in Smad6 confines BMP-induced Smad1 signaling. J. Biol. Chem. 296, 100496–100497. 10.1016/J.JBC.2021.100496. [PubMed: 33667543]
62. Wang Y, Hsu JM, Kang Y, Wei Y, Lee PC, Chang SJ, Hsu YH, Hsu JL, Wang HL, Chang WC, et al. (2016). Oncogenic functions of Gli1 in pancreatic adenocarcinoma are supported by its PRMT1-mediated methylation. Cancer Res. 76, 7049–7058. 10.1158/0008-5472.CAN-16-0715/652406/AM/ONCOGENIC-FUNCTIONS-OF-GLI-IN-PANCREATIC. [PubMed: 27758883]
63. Boj SF, Hwang CI, Baker LA, Chio IIC, Engle DD, Corbo V, Jager M, Ponz-Sarvise M, and Tiriac H (2015). and Spector MS. Organoid models of human and mouse ductal pancreatic cancer. Cell 160, 324–338. 10.1016/j.cell.2014.12.021. [PubMed: 25557080]
64. Croy BA, and Chapeau C (1990). Evaluation of the pregnancy immunotrophism hypothesis by assessment of the reproductive performance of young adult mice of genotype scid/scid.bg/bg. J Reprod Fertil 88, 231–239. 10.1530/jrf.0.0880231. [PubMed: 2313640]
65. Gu Z, Eils R, Schlesner M, and Ishaque N (2018). EnrichedHeatmap: An R/Bioconductor package for comprehensive visualization of genomic signal associations. BMC Genom. 19, 234–237. 10.1186/S12864-018-4625-X/FIGURES/2.
66. Subramanian A, Tamayo P, Mootha VK, Mukherjee S, Ebert BL, Gillette MA, Paulovich A, Pomeroy SL, Golub TR, Lander ES, and Mesirov JP (2005). Gene set enrichment analysis: a knowledge-based approach for interpreting genome-wide expression profiles. Proc Natl Acad Sci U S A 102, 15545–15550. 10.1073/pnas.0506580102. [PubMed: 16199517]
67. Heinz S, Benner C, Spann N, Bertolino E, Lin YC, Laslo P, Cheng JX, Murre C, Singh H, and Glass CK (2010). Simple Combinations of Lineage-Determining Transcription Factors Prime cis-Regulatory Elements Required for Macrophage and B Cell Identities. Mol. Cell 38, 576–589. 10.1016/j.molcel.2010.05.004. [PubMed: 20513432]
68. Robinson JT, Thorvaldsdóttir H, Winckler W, Guttman M, Lander ES, Getz G, and Mesirov JP (2011). Integrative genomics viewer. Nat Biotechnol 29, 24–26. 10.1038/nbt.1754. [PubMed: 21221095]
69. Ritchie ME, Phipson B, Wu D, Hu Y, Law CW, Shi W, and Smyth GK (2015). Limma powers differential expression analyses for RNA-sequencing and microarray studies. Nucleic Acids Res. 43, e47. 10.1093/nar/gkv007. [PubMed: 25605792]
70. Ianevski A, He L, Aittokallio T, and Tang J (2017). SynergyFinder: a web application for analyzing drug combination dose-response matrix data. Bioinformatics 33, 2413–2415. 10.1093/bioinformatics/btx162. [PubMed: 28379339]

Author Manuscript Author Manuscript Author Manuscript Author Manuscript

71. Wu J, Singh K, Lin A, Meadows AM, Wu K, Vivian Shing V, Bley M, Hassanzadeh S, Huffstutler RD, and Schmidt MS (2022). Boosting NAD+ blunts TLR4-induced type I IFN in control and systemic lupus erythematosus monocytes. J Clin Invest 132, e139828. 10.1172/JCI139828. [PubMed: 35025762]

72. Bioinformatics Babraham - FastQC A Quality Control tool for High Throughput Sequence Data https://www.bioinformatics.babraham.ac.uk/projects/fastqc/.

73. Langmead B, and Salzberg SL (2012). Fast gapped-read alignment with Bowtie 2. Nat. Methods 9, 357–359. 10.1038/nmeth.1923. [PubMed: 22388286]

74. Quinlan AR, and Hall IM (2010). BEDTools: a flexible suite of utilities for comparing genomic features. BIOINFORMATICS APPLICATIONS NOTE 26, 841–842. 10.1093/bioinformatics/btq033.

75. Lun ATL, and Smyth GK (2016). csaw: a Bioconductor package for differential binding analysis of ChIP-seq data using sliding windows. Nucleic Acids Res. 44, 45. 10.1093/nar/gkv1191. [PubMed: 26626151]

76. Gu Z, and Hübschmann D (2023). rGREAT: an R/bioconductor package for functional enrichment on genomic regions. Bioinformatics 39, btac745. 10.1093/BIOINFORMATICS/BTAC745. [PubMed: 36394265]

77. Love MI, Huber W, and Anders S (2014). Moderated estimation of fold change and dispersion for RNA-seq data with DESeq2. Genome Biol. 15, 550. 10.1186/s13059-014-0550-8. [PubMed: 25516281]

Author Manuscript Author Manuscript Author Manuscript Author Manuscript

Highlights

- Epigenetic reprogramming is associated with acquired chemoresistance
- PRMT1 is a central driver of acquired chemoresistance in PDAC
- PRMT1 inhibits chemo-induced chromatin recruitment of the MAFF/BACH1 complex
- PRMT1 gene signatures segregate PDAC patient survival and chemo response

Author Manuscript Author Manuscript Author Manuscript Author Manuscript

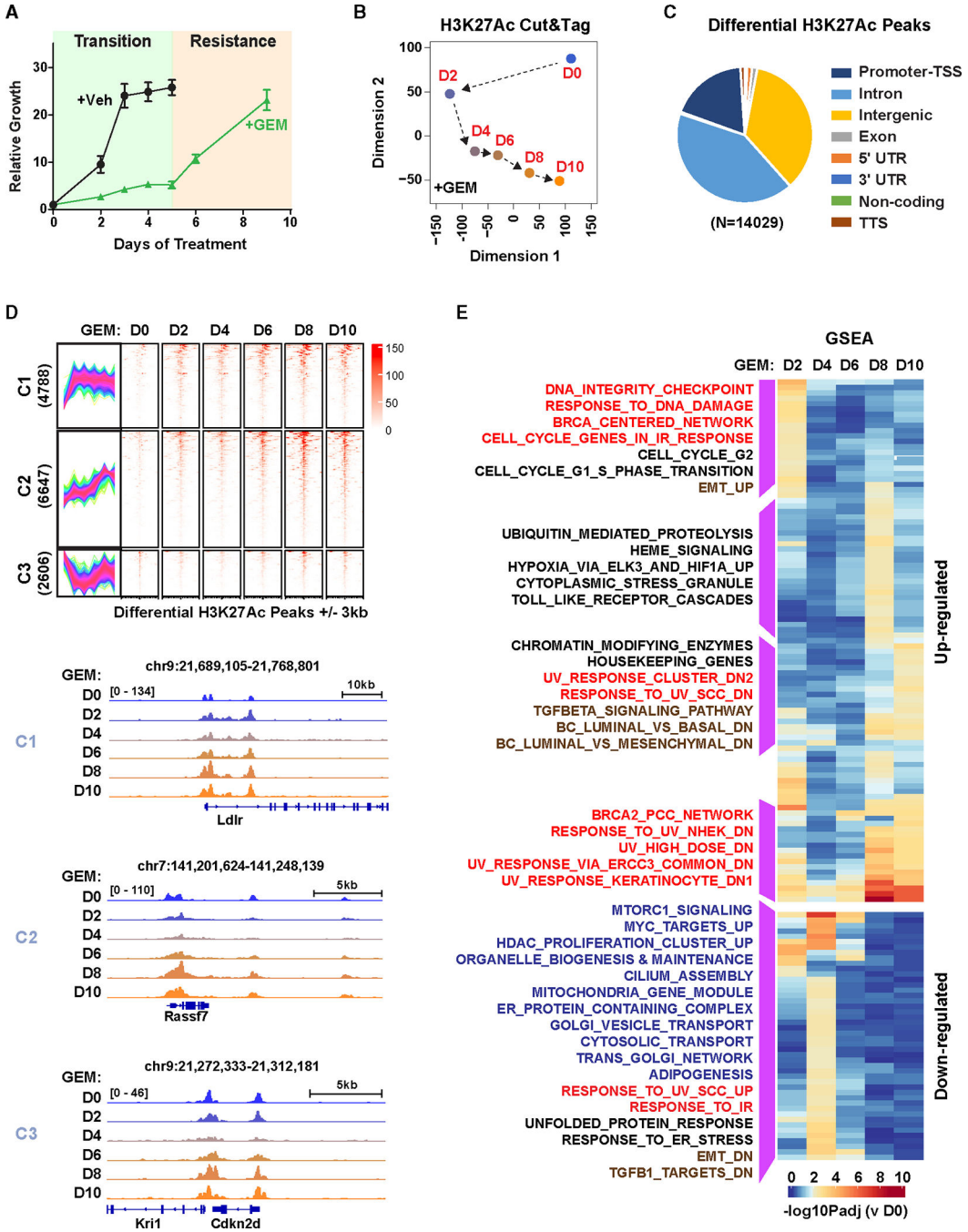

Figure 1. Gemcitabine treatment induces progressive epigenetic reprogramming in PDAC cells

(A) Cell proliferation assay of mT4 PDAC cells in the presence of vehicle control (+Veh, black) or gemcitabine (+GEM, green) over 10 days. Data are presented as mean values ± standard error (SE) of three independent experiments.

(B) Multidimensional-scaling (MDS) plot showing progressive changes in the overall H3K27Ac profiles in mT4 cells after indicated days of GEM treatment. Dissimilarity matrix is calculated using differential H3K27Ac peak signals between all time points (D0–D10) as determined by Cut&Tag (N = 14,029) and plotted using R limma package.

Author Manuscript Author Manuscript Author Manuscript Author Manuscript

(C) Pie graph summarizing the overlap frequencies of differential H3K27Ac peaks among all time points (D0–D10) with the indicated genomic features. TSS, transcription start site; UTR, untranslated region; TTS, transcription termination site.

(D) Fuzzy c-mean clustering (top left), corresponding heatmaps (top right), and representative genomic tracks (bottom) of differential H3K27Ac peaks between all time points (D0–D10). Differential peaks are segregated into three distinct profiles (C1–3) based on the relative signal changes from D0 to D10. Heatmaps depict H3K27Ac signals within ±3 kb of peak centers from all three clusters (top).

(E) Heatmaps showing −log10 adjusted *p* values (Padj) of significantly upregulated (top) or downregulated (bottom) gene sets in at least one GEM-treated time point (D2–D10) relative to baseline (D0) from gene set enrichment analysis (GSEA) of gene promoters with differential H3K27Ac signals (FC ≥ 2; adjusted $p \leq 0.05$).

Author Manuscript Author Manuscript Author Manuscript Author Manuscript

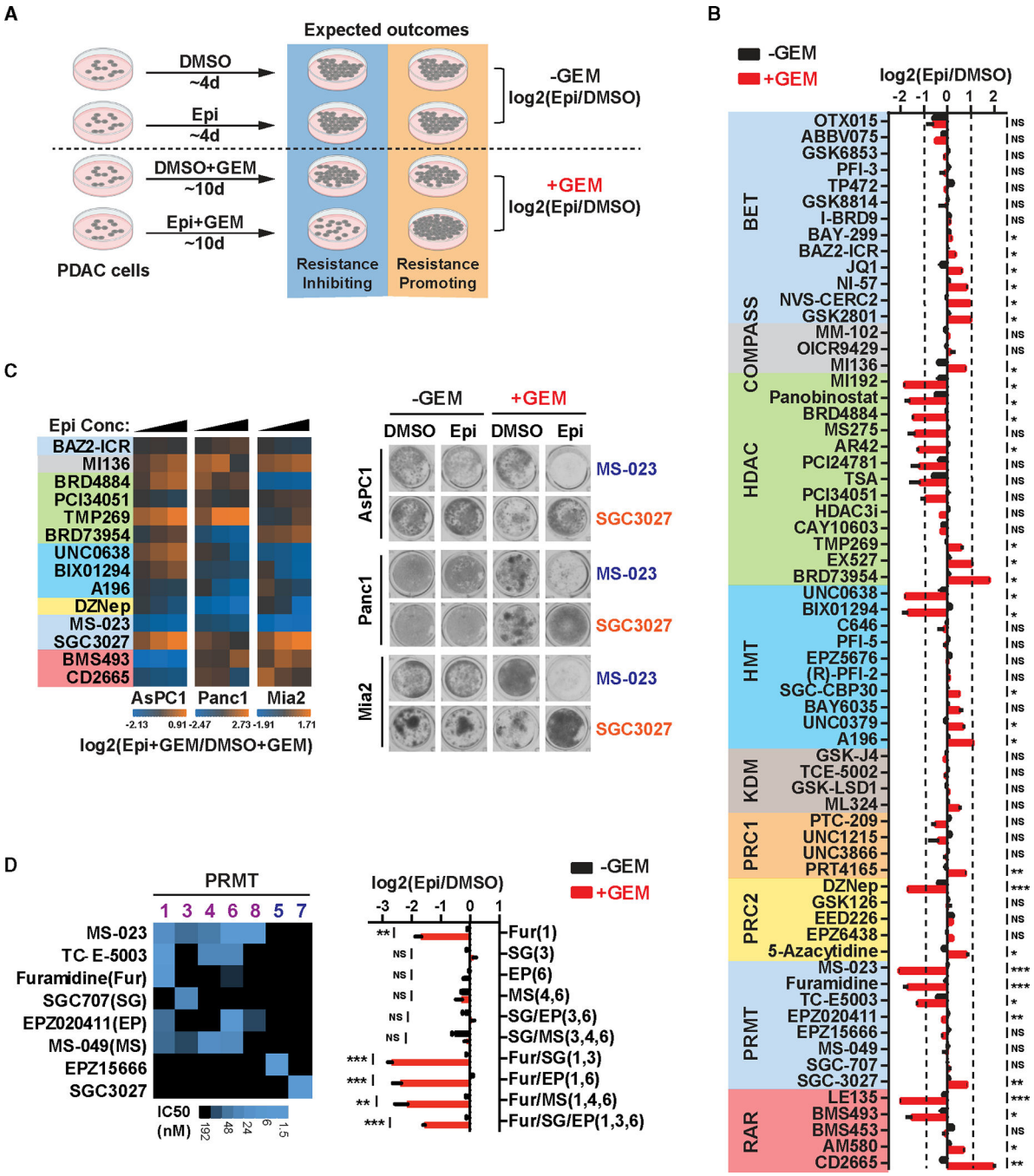

Figure 2. Epigenetic inhibitor screen identified PRMT1 as a potential driver of acquired gemcitabine resistance in PDAC cells

(A) Design of the epigenetic inhibitor (Epi) screen. mT4 PDAC cells were treated with DMSO control or sub-lethal doses of Epi in the presence (+GEM) or absence (−GEM) of GEM, then stained with crystal violet when DMSO controls reached ~70% confluence. Effects of Epi on cell growth were normalized to their respective DMSO controls in −GEM or +GEM conditions.

(B) Log2FC in cell densities of mT4 cells treated with indicated Epi compared to DMSO in the presence (+GEM, red bars) or absence (−GEM, black bars) of GEM as determined by

Author Manuscript Author Manuscript Author Manuscript Author Manuscript

crystal violet assays. Data presented are mean values ±SE of three independent experiments. *$p < 0.05$, **$p < 0.005$, ***$p < 0.0005$.

(C) Heatmaps showing log2 relative cell densities (left) and representative images (right) from crystal violet assays of AsPC1, Panc1, and MiaPaCa2 human PDAC cell lines treated with increasing concentrations of indicated Epi compared to DMSO in the presence of GEM ($N = 3$).

(D) Heatmap (left) showing reported half maximal inhibitory concentration (IC_{50}) values for inhibitors of PRMT class I (PRMT1, 3, 4, 6, 8, highlighted in purple), class II (PRMT5), and class III (PRMT7), and bar graph (right) showing log2FC in cell densities of mT4 cells treated with indicated Epi or combinations in the presence (+GEM, red bars) or absence (−GEM, black bars) of GEM as determined by crystal violet assays. Data presented are mean values ±SE of three independent experiments. *$p < 0.05$, **$p < 0.005$, ***$p < 0.0005$.

Author Manuscript Author Manuscript Author Manuscript Author Manuscript

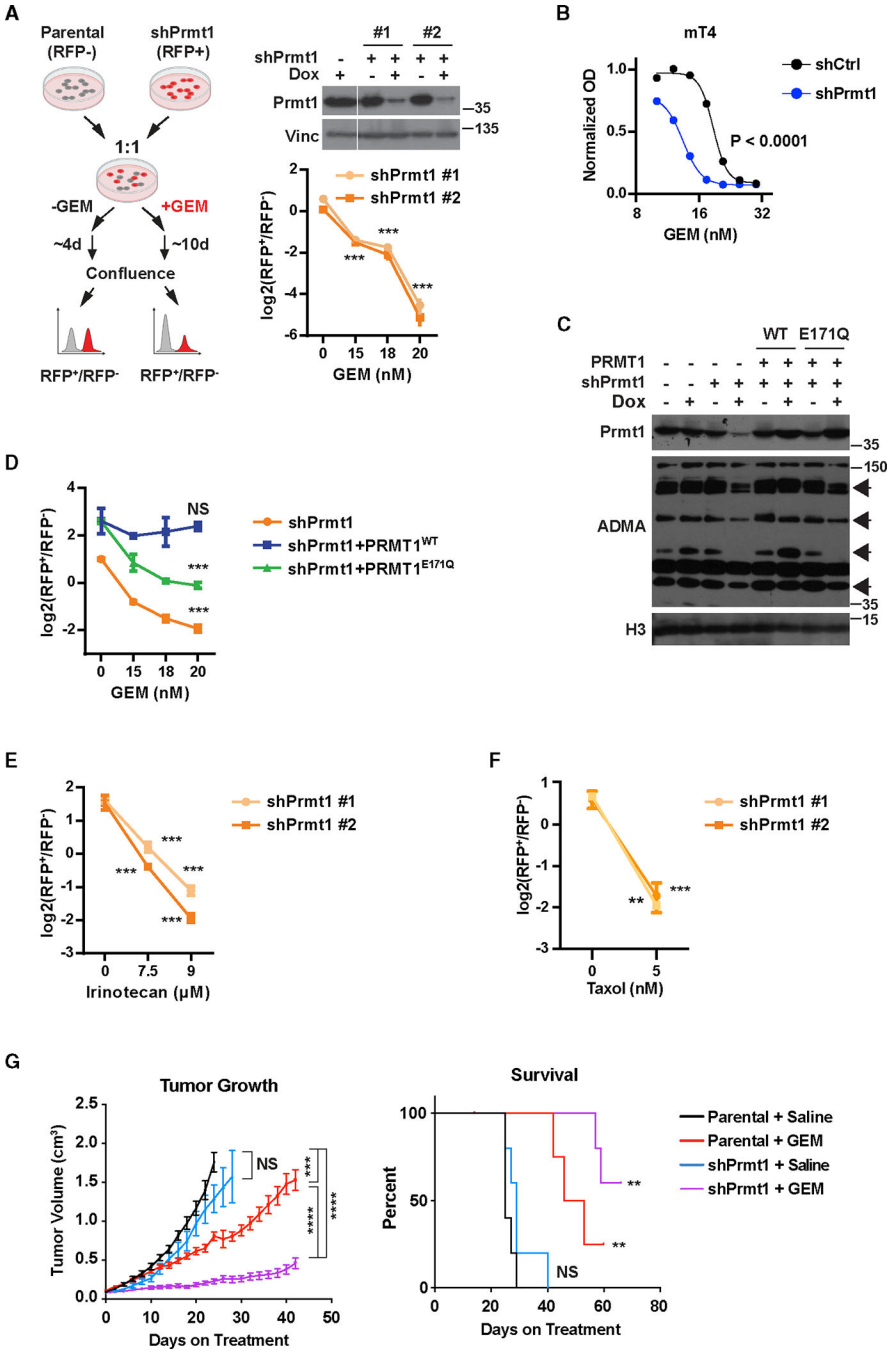

Figure 3. PRMT1 promotes the development of gemcitabine resistance in PDAC both *in vitro* and *in vivo*

(A) Experimental schematic (left), western blot (WB) confirmation (top right), and flow cytometry (FC) analysis of the log2 ratios (bottom right) of RFP-labeled (RFP+) mT4 cells expressing two different doxycycline (Dox)-inducible Prmt1 shRNAs (shPrmt1 #1 and #2) and unlabeled (RFP−) parental mT4 cells after co-culturing in the presence of indicated GEM concentrations. Vinc was used as loading control in WB. Blots shown in WB are representatives of at least three independent experiments; FC data presented are mean values ±SE of three independent experiments. ***$p < 0.0005$.

Author Manuscript Author Manuscript Author Manuscript Author Manuscript

(B) Normalized optical density (OD) of mT4 cells expressing shCtrl (black) and shPrmt1 (red) treated with increasing GEM concentrations as indicated. Fitted lines and statistical significance were determined by two-way ANOVA analysis (mixed model). Data shown are mean values ±SE of three independent experiments.

(C and D) WB analysis with indicated antibodies of total cell lysates (C) and FC analysis of the log2 ratios (D) of RFP-labeled (RFP+) mT4 cells expressing a Dox-inducible Prmt1 shRNA with or without reconstitution with wild-type (WT) or enzymatically dead mutant (E171Q) human PRMT1 relative to unlabeled (RFP−) parental mT4 cells. Histone 3 (H3) was used as loading control in (B). Arrows indicate ADMA-modified proteins downregulated by Prmt1 knockdown. Blots shown in WB are representatives of at least three independent experiments; FC data presented are mean values ±SE of three independent experiments. ***$p < 0.0005$. NS, not significant.

(E and F) FC analysis of the ratios of RFP-labeled (RFP+) mT4 cells expressing Dox-inducible shPrmt1 (#1 or #2) and unlabeled (RFP−) parental mT4 cells after co-culturing in the presence of indicated concentrations of irinotecan (E) or Taxol (F). Data presented are mean values ±SE of three replicates.

(G) Tumor growth rates (left) and Kaplan-Meier survival curve (right) of C57BL/6 mice subcutaneously injected with parental or shPrmt1-expressing mT4 cells after indicated days of treatment with saline control or GEM. Tumor volume was measured every 2 days and a mouse was randomly assigned to GEM or saline treatment once tumor volume reached 100 mm^3. Parental + saline (black line, $N = 5$), parental + GEM (red line, $N = 4$), shPrmt1 + saline (blue line, $N = 5$), and shPrmt1 + GEM (purple line, $N = 5$). Two-way ANOVA comparison for repeated measures was performed between each arm and log rank (Mantel-Cox) test was used to determine significant difference in survival relative to baseline control (parental + saline). *$p < 0.05$; **$p < 0.01$; ***$p < 0.001$; ***$p < 0.0001$; NS, not significant. Error bars indicate SE.

Author Manuscript Author Manuscript Author Manuscript Author Manuscript

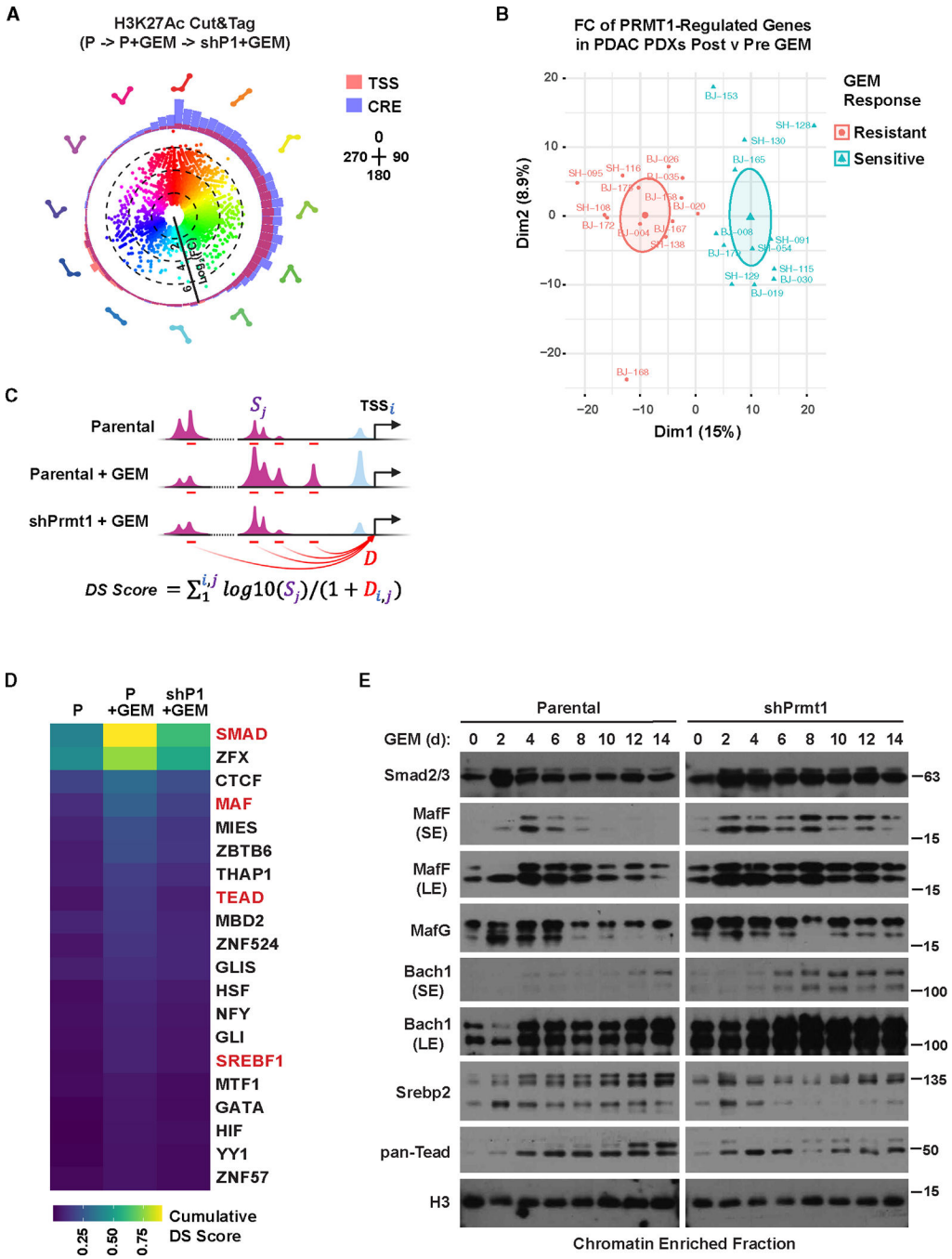

Figure 4. PRMT1 modulates gemcitabine-induced epigenetic reprogramming and dynamic changes in TF chromatin binding in PDAC cells

(A) Hue-saturation-value (HSV) transformation plot depicting differential H3K27Ac Cut&Tag peaks across untreated parental (P), GEM-treated parental (P + GEM), and GEM-treated shP1-expressing (shP1 + GEM) mT4 cells. Each data point represents a genomic region with significantly changed H3K27Ac signals and is colored and positioned based on the change pattern it displays from comparing the normalized Z scores across P → P + GEM → shP1 + GEM. The distance of each point from the center of the circle represents maximum absolute log2FC among the three conditions, and the color

Author Manuscript Author Manuscript Author Manuscript Author Manuscript

transparency represents the relative number of reads for that position. Outer histograms represent the densities of differential H3K27Ac peaks overlapping TSS or core-regulatory enhancer (CRE) across all angular positions.

(B) Principal-component analysis (PCA) based on RNA-seq analysis by Yang et al. of GEM-resistant (pink; $N = 13$) and GEM-sensitive (cyan; $N = 12$) human PDAC patient-derived xenografts (PDXs) stratified by fold change in mRNA expression prior to (pre) and after 3 weeks (post) of GEM treatment of genes whose TSS overlap with Prmt1-regulated, differential H3K27Ac peaks as determined by Cut&Tag.

(C) Schematic illustrating distance-signal (DS) score calculation for each transcription factor (TF) family: the sum of log10 transformed signals (S) of differential H3K27Ac CRE peaks that overlap the canonical motif of the TF family in question divided by their distances, D, to adjacent differential H3K27Ac TSS peaks as shown in (A). Sj represents the signal of a given differential H3K27Ac CRE peak overlapping a given motif j (red bar); Di,j represents the distance between a given differential H3K27Ac CRE peak overlapping the motif j and a given adjacent differential H3K27Ac TSS peak i.

(D) Heatmap showing cumulative DS scores of TFs with most differential cumulative DS scores in GEM-treated relative to untreated parental mT4 cells (P + GEM versus P) and between GEM-treated parental mT4 cells relative to GEM-treated mT4 cells expressing shPrmt1 (shP1 + GEM versus P + GEM).

(E) WB analysis with indicated antibodies of chromatin-enriched fractions from parental and shPrmt1-expressing mT4 cells following GEM treatment for indicated number of days (d). H3 was used as loading control. Blots shown are representatives of at least three independent experiments.

Author Manuscript Author Manuscript Author Manuscript Author Manuscript

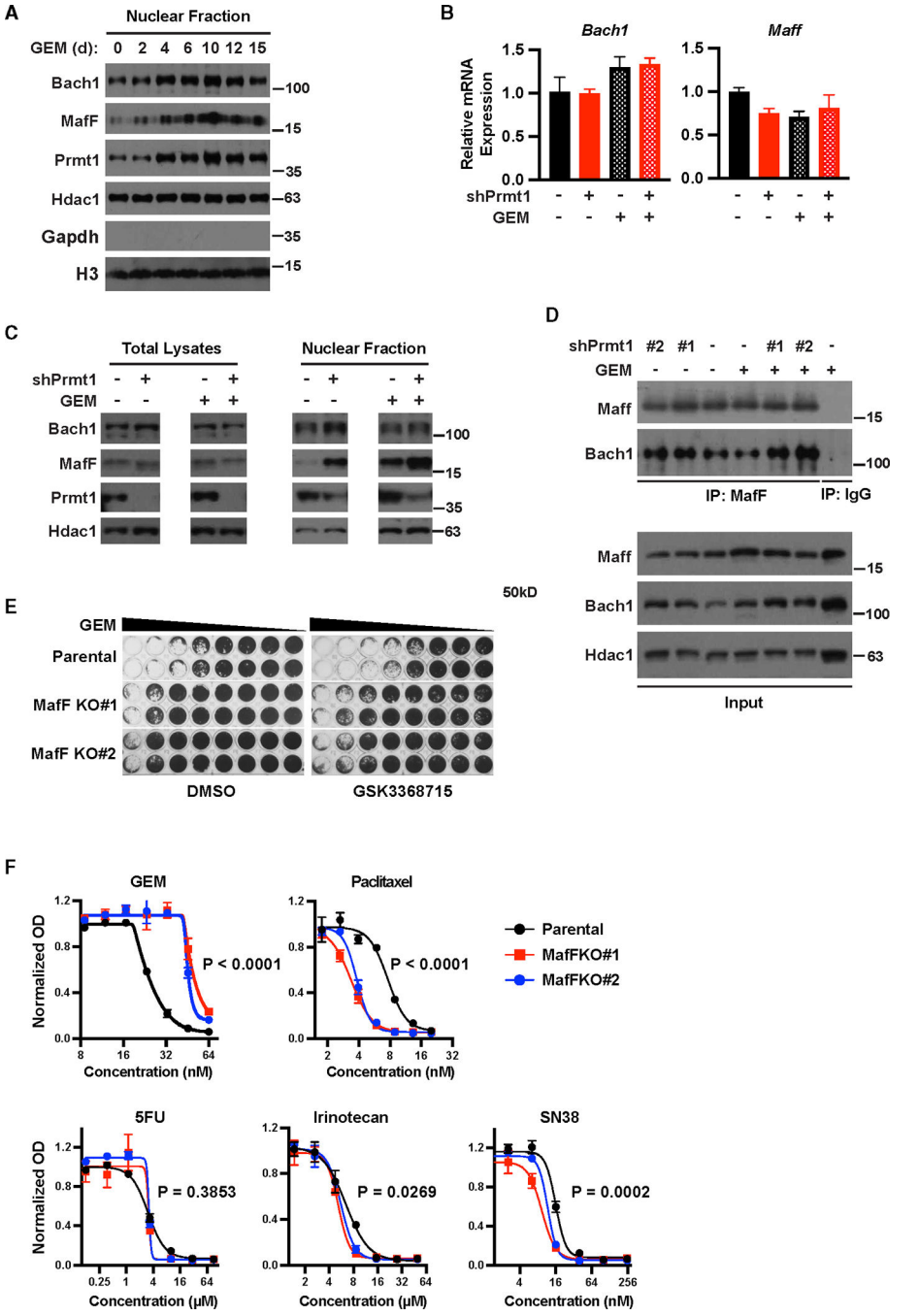

Figure 5. PRMT1 promotes acquired GEM resistance in part by inhibiting the nuclear accumulation of small MAF proteins and the assembly of MAF/BACH1 transcriptional complexes

(A) WB analysis with indicated antibodies of nuclear enriched fractions from mT4 cells subjected to indicated durations of GEM treatment. Hdac1 was used as overall loading control. Gapdh and H3 were used as markers for the cytoplasmic and chromatin fractions, respectively. Blots shown are representatives of at least three independent experiments.

Author Manuscript Author Manuscript Author Manuscript Author Manuscript

(B) Real-time quantitative reverse transcription PCR (qRT-PCR) analysis of relative MafF and Bach1 mRNA levels from parental or shPrmt1-expressing mT4 cells after 6 days of culturing with or without GEM. Data presented are mean values ±SE of three replicates.
(C) WB analysis with indicated antibodies of total cell lysates (left) and nuclear enriched fractions (right) from parental or shPrmt1-expressing mT4 cells after 6 days of culturing with or without GEM. Hdac1 was used as loading control. Blots shown are representatives of at least three independent experiments.
(D) WB analysis with indicated antibodies of immunoprecipitation (IP) with MafF or immunoglobulin (Ig) G antibody (top) and the corresponding inputs (bottom) from parental mT4 cells or mT4 cells expressing two different shPrmt1 shRNAs (shPrmt1 #1 and #2) after 6 days of culturing with or without GEM. Hdac1 was used as loading control. Blots shown are representatives of at least three independent experiments.
(E and F) Representative images (E) and normalized OD (F) of parental (black) or MafF-KO (#1, red; #2, blue) mT4 cells treated with increasing concentration GEM, paclitaxel, 5-FU, irinotecan, or SN38 as indicated. Fitted lines and statistical significance were determined by two-way ANOVA analysis (mixed model). Shown is mean value ±SD of two independent experiments.

Author Manuscript Author Manuscript Author Manuscript Author Manuscript

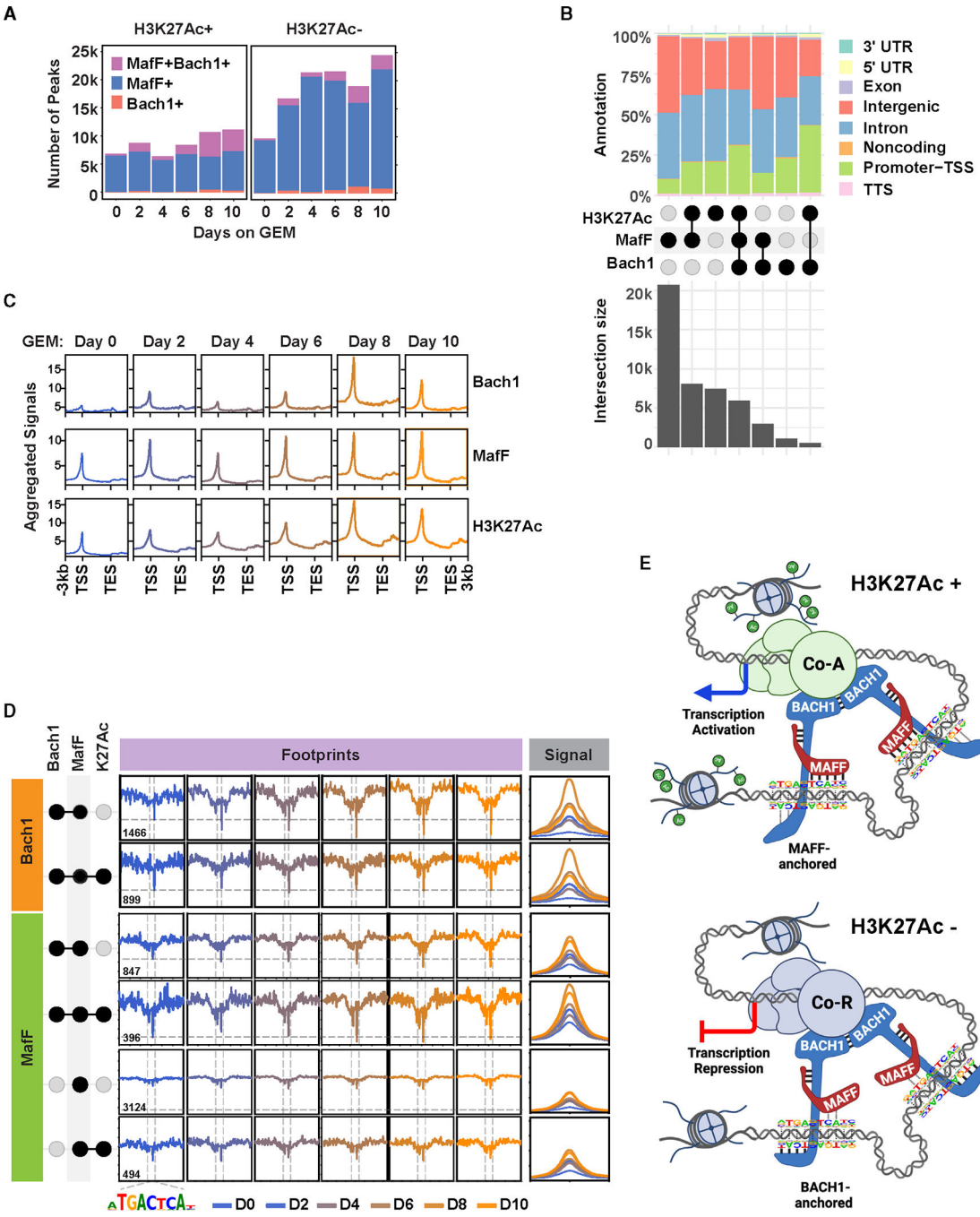

Figure 6. MAFF and BACH1 may play a major role in gemcitabine-induced epigenetic reprogramming

(A) Summary of the numbers of H3K27Ac+ or H3K27Ac− genomic loci bound by both MafF and Bach1 (MafF+Bach1+, purple), MafF alone (MafF+, blue), or Bach1 alone (Bach1+, orange) in mT4 cells at indicated time points (D0, 2, 4, 6, 8, 10) of GEM treatment, as detected by Cut&Tag.

(B) Summary of the total numbers of genomic loci in mT4 cells that overlap with H3K27Ac, MafF, and/or Bach1 Cut&Tag peaks at one or more time points of GEM treatment (bottom)

Author Manuscript Author Manuscript Author Manuscript Author Manuscript

and their frequencies of overlap with the indicated genome features (top). Black and gray dots indicate positive and negative overlaps, respectively.

(C) Aggregated Bach1, MafF, and H3K27Ac Cut&Tag signals within ±3 kb from of all known gene bodies (TSS-TTS) in mT4 cells at indicated time points of GEM treatment.

(D) Aggregated Tn5-bias-corrected footprint (left) and signal (right) profiles within ±60 bp from the centers of the genomic sites matching the MAFK_MA0496.3 JASPAR motif from Bach1 (top) and MafF (bottom) Cut&Tag peaks grouped according to the statuses of overlap with each other and H3K27Ac at indicated time points of GEM treatment. Black and gray dots indicate positive and negative overlaps, respectively.

(E) A working model of cooperative binding between MAFF and BACH1 that drives transcription activation or repression.

Author Manuscript Author Manuscript Author Manuscript Author Manuscript

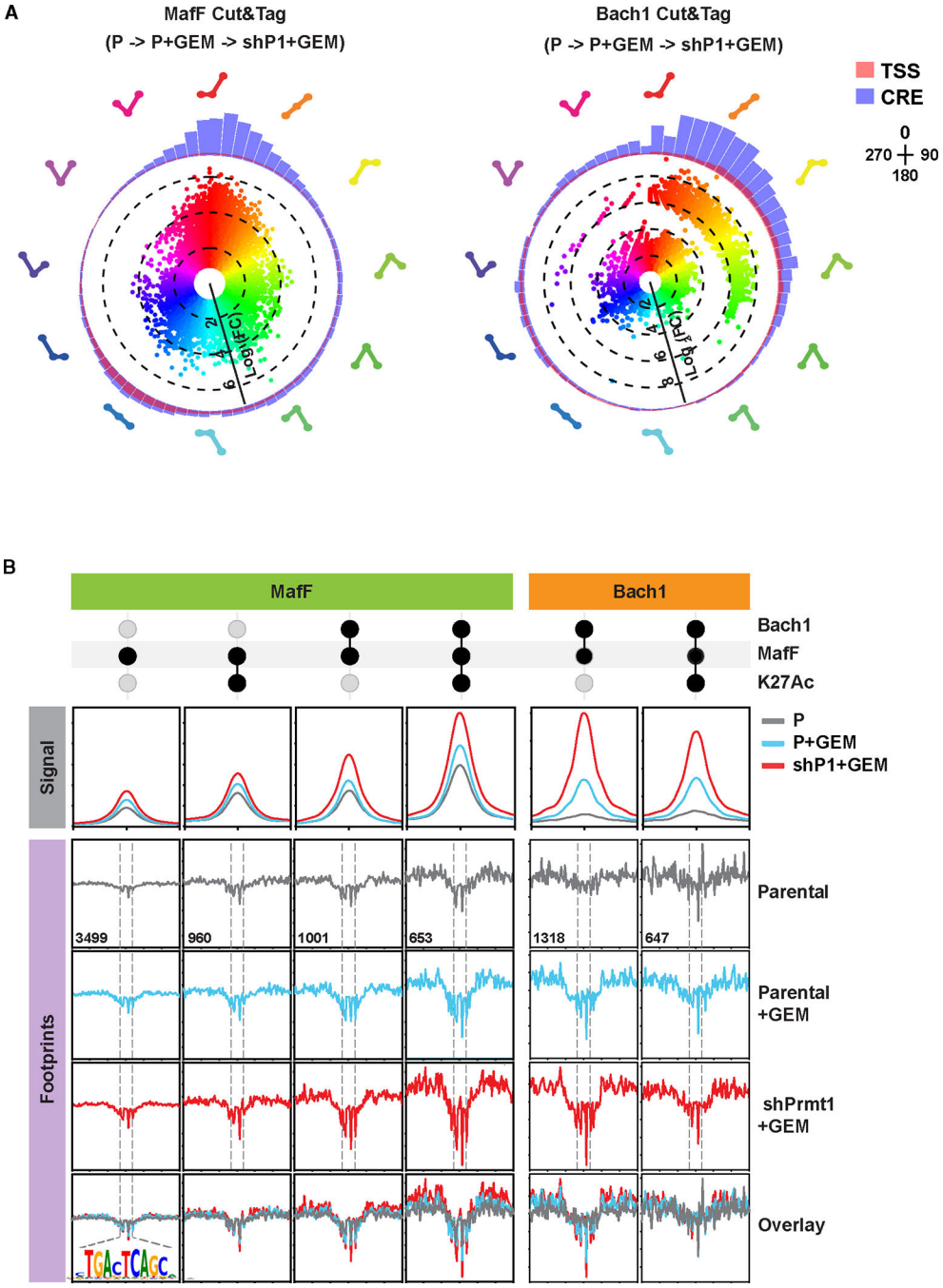

Figure 7. PRMT1 prevents the chromatin overloading of the MAFF/BACH1 transcriptional complexes in response to gemcitabine

(A) HSV transformation plot depicting differential MafF (left) and Bach1 (right) peaks across untreated parental (P), GEM-treated parental (P + GEM), and GEM-treated shP1-expressing (shP1 + GEM) mT4 cells. Each data point represents a significantly changed peak and is colored based on the pattern it displays comparing the normalized *Z* scores across P / P + GEM / shP1 + GEM. The distance of each point from the center of the circle represents maximum log2FC among the three conditions, and the color transparency represents the relative number of reads for that data point. Outer histograms represent the

densities of differential MafF or Bach1 peaks overlapping TSS or CRE across all angular positions.

(B) Aggregated signal (top) and Tn5-bias-corrected footprint (bottom) profiles within ±60 bp from the centers of the genomic sites matching the Bach1-Mafk_MA0591.1 JASPAR motif from MafF (left) and Bach1 (right) Cut&Tag peaks grouped according to the statuses of overlap with each other and H3K27Ac in untreated parental (P, gray line), GEM-treated parental (P + GEM, blue line), and GEM-treated shP1-expressing (shP1 + GEM, red line) mT4 cells. Black and gray dots indicate positive and negative overlaps, respectively.

Author Manuscript Author Manuscript Author Manuscript Author Manuscript

Author Manuscript Author Manuscript Author Manuscript Author Manuscript

KEY RESOURCES TABLE

REAGENT or RESOURCE	SOURCE	IDENTIFIER
Antibodies		
Goat polyclonal anti-tdTomato	LifeSpan	Cat#LS-C348313
Mouse monoclonal Anti-E-Cadherin	BD Biosciences	Cat#610182; RRID:AB_397581
Rabbit polyclonal anti-PRMT1	Proteintech	Cat#11279–1-AP; RRID:AB_2171319
Rabbit monoclonal anti-pH2AX	Cell Signaling Technology	Cat#9718S; RRID:AB_2118009
Rabbit monoclonal anti-RPA32/RPA2	Cell Signaling Technology	Cat#35869; RRID:AB_2799086
Rabbit monoclonal anti-NF-kb p65	Cell Signaling Technology	Cat#8242; RRID:AB_10859369
Rabbit monoclonal anti-ADMA	Cell Signaling Technology	Cat#13522; RRID:AB_2665370
Anti-acetyl-Histone H3 (Lys27) Antibody	Millipore	Cat#07–360; RRID:AB_310550
Anti-trimethyl-Histone H3 (Lys4) Antibody	Millipore	Cat#07–473; RRID:AB_1977252
Rabbit polyclonal anti-H3	Proteintech	Cat#17168–1-AP; RRID:AB_2716755
Rabbit polyclonal anti-HDAC1	Proteintech	Cat#10197–1-AP; RRID:AB_2920338
Mouse monoclonal anti-Vinculin (Clone 7F9)	Santa Cruz Biotechnology	Cat#sc-73614; RRID:AB_1131294
Mouse monoclonal anti-b-Actin (Clone C4)	Santa Cruz Biotechnology	Cat#sc-47778; RRID:AB_2714189
Rabbit polyclonal anti-MAFF	Proteintech	Cat#12771–1-AP; RRID:AB_2137677
Rabbit polyclonal anti-BACH1	Proteintech	Cat#14018–1-AP; RRID:AB_2274498
Rabbit polyclonal anti-SMAD2/3	Cell Signaling Technology	Cat#3102; RRID:AB_10698742
Rabbit polyclonal anti-MAFG	Novus Biological	Cat#NBP2–15019; RRID:AB_2297120
Rabbit polyclonal anti-SREBP2	Proteintech	Cat#14508–1-AP; RRID:AB_2194235
Rabbit monoclonal anti-pan-TEAD	Cell Signaling Technology	Cat#13295; RRID:AB_2687902
Rabbit polyclonal anti-HIF1a	Abcam	Cat#ab82832; RRID:AB_1860665
Rabbit polyclonal anti-HIF2a (EPAS1)	Novus Biological	Cat#NB100–122; RRID:AB_10002593
c-Jun (60A8) Rabbit mAb antibody	Cell Signaling Technology	Cat#9165; RRID:AB_2130165
Anti-rabbit IgG, HRP-linked Antibody	Cell Signaling Technology	Cat#7074; RRID:AB_2099233
Anti-mouse IgG, HRP-linked Antibody	Cell Signaling Technology	Cat#7076; RRID:AB_330924
Chemicals, peptides, and recombinant proteins		
(R)-PFI-2	Cayman	Cat#14678; CAS: 1627607–87-7
5-Azacytidine	ApexBio	Cat#A1907; CAS: 320–67-2
5-FluoroUracil (5-FU)	Cayman	Cat#0499389–18; CAS: 51–21-08
A-196	Cayman	Cat#18317; CAS: 1982372–88-2
ABBV-075	Cayman	Cat#21033; CAS: 1445993–26-9
AM580	Cayman	Cat#15261; CAS: 102121–60-8
AMI-1	Cayman	Cat#13965; CAS: None
AR-42	Cayman	Cat#17531; CAS: 1798310–55-0
AZD 6738	Cayman	Cat#21035; CAS: 1352226–88-0
BAY-299	Cayman	Cat#19777; CAS: 2080306–23-4
BAY-6035	Cayman	Cat#25925; CAS: 2247890–13-5
BAY-850	MedChemExpress	Cat#HY-119254; CAS: 2099142–76-2

Author Manuscript Author Manuscript Author Manuscript Author Manuscript

REAGENT or RESOURCE	SOURCE	IDENTIFIER
BAZ2-ICR	Cayman	Cat#17448; CAS: 1665195–94-7
BIX 01294	Cayman	Cat#13124; CAS: 1808255–64-2
Blasticidin	Thermo Fisher Scientific	Cat#A1113903
BMS 453	Cayman	Cat#19076; CAS: 166977–43-1
BMS493	Cayman	Cat#17418; CAS: 215030–90-3
BRD4884	Cayman	Cat#19834; CAS: 1404559–91-6
BRD73954	Cayman	Cat#16919; CAS: 1440209–96-0
C646	Cayman	Cat#10549; CAS: 328968–36-1
CAY10603	Cayman	Cat#13146; CAS: 1045792–66-2
CD2665	Cayman	Cat#16031; CAS: 170355–78-9
Doxycycline hydrochloride	Alfa Aesar	Cat#J60422; CAS: 10592–13-9
DZNep	Cayman	Cat#13828; CAS: 102052–95-9
EED226	Cayman	Cat#22031; CAS: 2083627–02-3
EPZ015666	Cayman	Cat#17285; CAS: 1616391–65-1
EPZ020411	Cayman	Cat#19160; CAS: 1700663–41-7
EPZ5676	Cayman	Cat#16175; CAS: 1380288–87-8
EPZ6438	Cayman	Cat#16174; CAS: 1403254–99-8
EX-527	Cayman	Cat#10009798; CAS: 49843–98-3
Flavopiridol	Selleck Chemical	Cat#S1230; CAS:146426–40-6
Furamidine	Cayman	Cat#19121; CAS: 55368–40-6
Gemcitabine	AdooQ	Cat#A10423; CAS: 95058–81-4
Gemcitabine	ApexBio	Cat#A1402; CAS: 95058–81-4
GSK126	Cayman	Cat#15415; CAS: 1346574–57-9
GSK2801	Cayman	Cat#14120; CAS: 1619994–68-1
GSK3368715	MedChemExpress	Cat#HY-128717A; CAS: 2227587–25-7
GSK-4027	MedChemExpress	Cat#HY-101027; CAS: 2079896–25-4
GSK484	Cayman	Cat#17488; CAS: 1652591–81-5
GSK6853	Cayman	Cat#20985; CAS: 1910124–24-1
GSK-8814	MedChemExpress	Cat#HY-114204; CAS: 1997369–78-4
GSK-J4	Cayman	Cat#12073; CAS: 1797983–09-5
GSK-LSD1	Cayman	Cat#16439; CAS: 2102933–95-7
HDAC3i	Cayman	Cat#21057; CAS: 2044701–99-5
HMN-214	AdooQ	Cat#A10452–10; CAS: 173529–46-9
Hygromycin	Thermo Fisher Scientific	Cat#10687010
I-BRD9	Cayman	Cat#17749; CAS: 1714146–59-4
Irinotecan	Cayman	Cat#14180; CAS: 136572–09-3
JIB-04	Cayman	Cat#15338; CAS: 199596–05-9
JQ1	Cayman	Cat#11187; CAS: 1268524–70-4
Ku-60019	Cayman	Cat#17502; CAS: 925701–46-8
LE 135	Cayman	Cat#14415; CAS: 155877–83-1
LY2606368	Cayman	Cat#21490; CAS:1234015–52-1
MI-136	Cayman	Cat#19245; CAS: 1628316–74-4

Author Manuscript Author Manuscript Author Manuscript Author Manuscript

REAGENT or RESOURCE	SOURCE	IDENTIFIER
MI192	Cayman	Cat#18288; CAS: 1415340–63-4
MK-1775	Cayman	Cat#21266; CAS: 955365–80-7
ML-324	Cayman	Cat#17472; CAS: 1222800–79-4
MM-102	Cayman	Cat#17699; CAS: 1417329–24-8
MRK-740	MedChemExpress	Cat#HY-114209; CAS: 2387510–80-5
MS023	Cayman	Cat#34786; CAS: 1831110–54-3
MS049	Cayman	Cat#HY-100360/18348; CAS: 2095432–59-8
MS-275	Cayman	Cat#13284; CAS: 209783–80-2
Nextrastat A	Cayman	Cat#71462653; CAS No.1403783–31-2
NI-57	Cayman	Cat#17662; CAS: 1883548–89-7
NVS-CECR2–1	Cayman	Cat#18316; CAS: 1992047–61-6
OICR-9429	Cayman	Cat#16095; CAS: 1801787–56-3
OTX015	Cayman	Cat#15947; CAS: 202590–98-5
Oxaliplatin	Cayman	Cat#13106; CAS: 61825–94-3
Paclitaxel	Cayman	Cat#10461; CAS: 33069–62-4
Panobistat	MedChemExpress	Cat#HY-10224; CAS: 404950–80-7
PCI 34051	Cayman	Cat#10444; CAS: 950762–95-5
PCI24781	Cayman	Cat#20059; CAS: 783355–60-2
PFI-3	Cayman	Cat#15267; CAS: 1819363–80-8
PFI-5	Cayman	Cat#15267; CAS: 1819363–80-8
PRT4165	Cayman	Cat#19093; CAS: 31083–55-3
PTC-209	Cayman	Cat#16277; CAS: 315704–66-6
Puromycin	Thermo Fisher Scientific	Cat#A1113803
SCH 900776	Cayman	Cat#18131; CAS: 891494–63-6
SGC3027	SGC	Cat#6825; CAS:None
SGC707	Cayman	Cat#17017; CAS: 1687736–54-4
SGC-CBP30	Cayman	Cat#14469; CAS: 1613695–14-9
TC-E 5002	Cayman	Cat#17717; CAS: 1453071–47-0
TC-E 5003	Cayman	Cat#17718; CAS: 17328–16-4
TMP269	Cayman	Cat#17738; CAS: 1314890–29-3
TP-472	Cayman	Cat#20030; CAS: 2079895–62-6
Trichostatin A	Cayman	Cat#89730; CAS: 58880–19-6
UNC0379	Cayman	Cat#16400; CAS: 1620401–82-2
UNC0638	Cayman	Cat#10734; CAS: 1255580–76-7
UNC1215	Cayman	Cat#13968; CAS: 1415800–43-9
UNC3866	Cayman	Cat#19237; CAS: 1872382–47-2
Critical commercial assays		
GoTaq® Green Master Mix	Promega	Cat#M7122
iScript cDNA Synthesis Kit	Bio-Rad	Cat#1708890
iTaq Universal SYBR Green Supermix	Bio-Rad	Cat#1725124
Pierce BCA Protein Assay Kit	Thermo Fisher Scientific	Cat#23225

Author Manuscript Author Manuscript Author Manuscript Author Manuscript

REAGENT or RESOURCE	SOURCE	IDENTIFIER
PrepEase Genomic DNA isolation kit	Affymetrix	Cat#78855
Gateway™ BP Clonase™ II Enzyme mix	Thermo Fisher Scientific	cat# 11789020
Forget-Me-Not EvaGreen qPCR mastermix	Biotium	cat# 31041–1
Gateway LR Clonase II Plus	Thermo Fisher Scientific	cat# 11791020
AccuGel Acylamide-Bis-Acrylamid	National Diagnostics	Cat# EC-849
RNAeasy Mini Kit	Qiagen	Cat#74104
Lipofectamine 2000	Thermo Fisher Scientific	cat# 12566014
anti-V5 Beads	Sigma-Aldrich	Cat#021M4839
α-Protein-G Agarose beads	Millipore	cat# 16–201
EZview Red anti-HA gel	Sigma-Aldrich	Cat#E6779
NEBNext HiFi 2x PCR Master mix	NEB	Cat#M0541
BioMag®Plus Concanavalin A	Bangs Laboratories	Cat#BP531
Mag-Bind® TotalPure NGS beads	Omega Bio Tech	Cat#M1378
Deposited data		
Cut&Tag Sequencing Data	NCBI Gene Expression Omnibus (GEO)	GEO: GSE227129
Experimental models: Cell lines		
Panc1	ATCC	CRL-1469
AsPC1	ATCC	CRL-1682
MiaPaCa2	ATCC	CRM-CRL-1420
293T	ATCC	CRL-3216
mT4	Sylvia F.Boj et al., 2015[63]	N/A
HPAF-II	ATCC	CRL-1997
Capan-1	ATCC	HTB79
Experimental models: Organisms/strains		
Mouse line: CL57/BL6	Charles River Laboratories (Croy and Chapeau, 1990[64])	Strain code #027
Mouse line: NOD.Cg-Prkdc^{scid}/J	The Jackson Laboratory	Strain#: 001303
Oligonucleotides		
See Table S4 for Oligonucleotides with sequences		N/A
Recombinant DNA		
LentiCrispr v2 (TLCv2)	Addgene	Cat#52961
pCW57-MafF-WT	This paper	N/A
pCW57-MCS1–2A-MCS2	Addgene	Cat##71782
pCW57-Prmt1-E171Q	This paper	N/A
pCW57-Prmt1-WT	This paper	N/A

Author Manuscript Author Manuscript Author Manuscript Author Manuscript

REAGENT or RESOURCE	SOURCE	IDENTIFIER
pTRIPZ lentiviral vector	GE Healthcare Dharmacon, Inc.	Cat#RHS4740
pTRIPZ -shPrmt1#1	This paper	N/A
pTRIPZ -shPrmt1#2	This paper	N/A
TLCv2-gMafF	This paper	N/A
Software and algorithms		
EnrichedHeatmap	Gu et al.[65]	https://bioconductor.org/packages/devel/bioc/vignettes/EnrichedHeatmap/inst/doc/EnrichedHeatmap.html
FCS Express 7	*Denovo* Software, Dotmatics	N/A
Gene Set Enrichment Analysis	Subramaniana et al., 2005[66]; Mootha et al.[16]	http://software.broadinstitute.org/gsea/index.jsp
GREAT version 3.0.0	McLean et al.[13]	http://great.stanford.edu/public/html/news.php
HOMER	Heinz et al.[67]	http://homer.ucsd.edu/homer/
IGV	Robinson et al., 2011[68]	https://software.broadinstitute.org/software/igv/
ImageJ (Fiji)	NIH	https://imagej.net/software/fiji/
Limma	Ritchie et al.[69]	https://bioconductor.org/packages/release/bioc/html/limma.html
pHeatmap		https://cran.r-project.org/web/packages/pheatmap/index.html
PRISM	Graphpad, Dotmatics	N/A
R version 4.0.4	The R Foundation for Statistical Computing	https://www.r-project.org/
SynergyFinder 1.0	Ianevski et al., 2017[70]	https://synergyfinder.fimm.fi
TCseq	Wu et al., 2022[71]	https://bioconductor.org/packages/release/bioc/vignettes/TCseq/inst/doc/TCseq.pdf
TOBIAS	Bentsen et al.[59]	https://github.molgen.mpg.de/pages/loosolab/www/software/TOBIAS/